

# No Labels, No Look-Ahead: Unsupervised Online Video Stabilization with Classical Priors

Tao Liu<sup>1\*</sup> Gang Wan<sup>1</sup> Kan Ren<sup>1†</sup> Shibo Wen<sup>2\*</sup>

<sup>1</sup>School of Electronic and Optical Engineering, Nanjing University of Science and Technology

<sup>2</sup>College of Geoexploration Science and Technology, Jilin University

liutao23@njust.edu.cn, wangang@njust.edu.cn, K.ren.@njust.edu.cn, wensb23@mails.jlu.edu.cn

## Abstract

We propose a new unsupervised framework<sup>1</sup> for online video stabilization. Unlike methods based on deep learning that require paired stable and unstable datasets, our approach instantiates the classical stabilization pipeline with three stages and incorporates a multithreaded buffering mechanism. This design addresses three longstanding challenges in end-to-end learning: limited data, poor controllability, and inefficiency on hardware with constrained resources. Existing benchmarks focus mainly on handheld videos with a forward view in visible light, which restricts the applicability of stabilization to domains such as UAV nighttime remote sensing. To fill this gap, we introduce a new multimodal UAV aerial video dataset (UAV-Test). Experiments show that our method consistently outperforms state-of-the-art online stabilizers in both quantitative metrics and visual quality, while achieving performance comparable to offline methods.

## 1. Introduction

Video stabilization is a common requirement in both amateur and professional video capture, aiming to suppress unintended camera shake and enhance visual quality. To avoid the high cost and operational complexity of physical stabilizers, researchers have proposed a wide range of algorithmic solutions. Classical approaches typically follow a three-stage pipeline: motion estimation, motion smoothing, and stabilized frame generation. Based on the dimensionality of the motion model, these methods can be classified as 2D, 2.5D, or 3D. 2D methods adopt affine transformations [13], homographies [33], or optical flow [27, 56], achieving high efficiency but struggling with parallax and depth variations. 2.5D approaches [25, 51] incorporate lim-

ited 3D cues from feature trajectories to mitigate parallax, but remain computationally expensive. 3D methods leverage depth sensors [23], reconstructed point clouds [24], or epipolar geometry [12] to address complex scenes effectively, but entail significant computational overhead.

Deep learning enables end-to-end stabilization by directly generating stabilized frames from shaky inputs. However, such frameworks are often difficult to interpret or control and typically rely on large paired datasets of stable/unstable videos. In practice, unavoidable temporal and spatial misalignments make available data prone to parallax effects [48], limited scenario coverage [57], and synthetic-to-real gaps [22]. Recent studies, therefore, explore a decoupled design. DUT [52] augments the classical pipeline with neural motion propagation and smoothing, achieving strong stabilization. Nevertheless, it remains constrained by its network architecture [44] and a global smoothing strategy, and therefore operates offline. Another line of work [58] leverages high-quality motion-estimation networks [53] and focuses on optimizing the smoothing module, thereby enabling online stabilization. Yet, the lack of open-source motion estimators and reduced robustness in complex scenes still pose significant challenges.

Our literature review and empirical analysis highlight three key limitations common to both classical and learning-based stabilizers:

- **Perception Limitations:** Classical methods rely on handcrafted keypoint detectors [31, 36, 37], which struggle with weak textures, occlusions, and large motions, leading to biased motion estimation [26]. Although deep learning methods [60] improve robustness, they lack interpretability and controllability, limiting their adaptability to real-world scenarios.
- **Smoothing Limitations:** Classical methods employ fixed smoothing strategies [29], which fail to generalize well, resulting in residual jitter [28]. Learning-based smoothing methods lack geometric interpretability [7], thereby risking over-smoothing or distortion [48].
- **Online Processing Limitations:** Many stabilizers, both

\*Equal contribution

†Corresponding author

<sup>1</sup><https://github.com/liutao23/LightStab.git>.

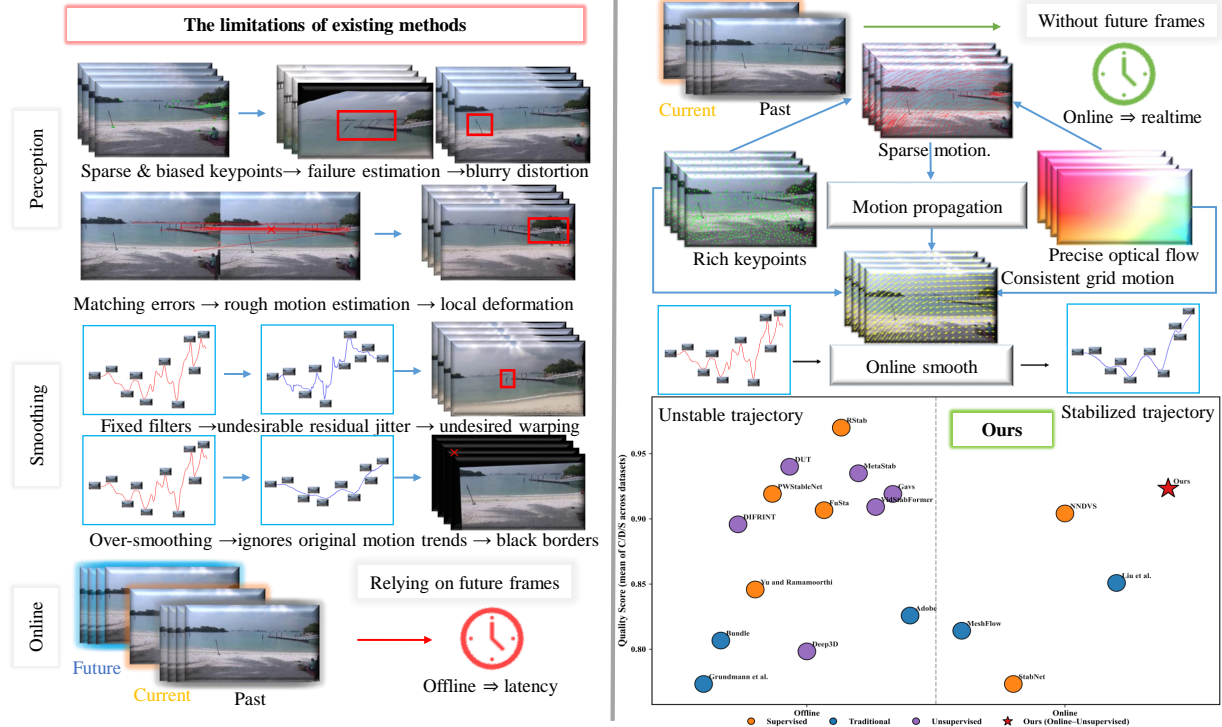


Figure 1. Limitations of existing methods and an overview of our approach. (a) Traditional pipelines rely on sparse, spatially biased keypoints, leading to inaccurate motion estimation and blur/distortion in stabilized frames. (b) Over-smoothing and fixed filtering ignore scene motion trends, resulting in residual jitter, black borders, and warping in the output video. (c) Our approach uses dense, evenly distributed keypoints together with accurate optical flow to propagate motion estimates across frames; it operates online without future frames, enabling real-time processing. (d) In the bottom-right chart, our method (red star) outperforms both traditional offline methods and recent online methods in stabilization quality, achieving state-of-the-art performance for online unsupervised stabilization.

classical and learning-based, are not designed for on-line processing and rely on offline aggregation or batch processing, introducing delays. Additionally, learning-based methods require large labeled datasets and significant computational resources [48], hindering online deployment.

As shown in Fig. 1, existing stabilizers face challenges in motion perception and trajectory smoothing, which often lead to artifacts under complex conditions, and are mostly limited to offline processing. To address these challenges, we propose the following solutions. For **Motion Perception**, we combine multi-detector collaboration with keypoint uniformization to enhance robustness, reduce optical flow overhead, and introduce an efficient motion propagation network to maintain global motion consistency. In terms of **Trajectory Smoothing**, we present an online dynamic-kernel optimization method that avoids fixed filters and future-frame dependencies, enabling online stabilization with improved control. For **System Design**, we implement a multi-threaded asynchronous pipeline that decouples and parallelizes core modules, reducing latency and enabling high-frame-rate processing.

In summary, our framework combines robust motion perception, interpretable trajectory smoothing, and efficient system design into a **simulation-informed stabilization chain**, which overcomes existing limitations in perception, analysis, and online performance. The main contributions of this work are as follows:

- We propose a novel unsupervised online video stabilization model that removes the need for paired training data while enabling online processing of unstable videos.
- We introduce **UAV-Test**, a realistic multimodal dataset of unstable aerial videos covering diverse drone-shake scenarios, intended as a benchmark for related research, to be released upon acceptance.
- Extensive experiments on public and newly collected datasets show that our method surpasses state-of-the-art online stabilizers in quality and achieves performance on par with offline approaches.

## 2. Related Work

### 2.1. Video Stabilization

Traditional video stabilization methods [13, 26] suppress screen jitter by estimating camera motion trajectories and applying smoothing techniques, or by using adaptive sparse grids for real-time performance [28]. However, these methods often rely on manually designed feature detectors, which may lead to uneven keypoint distribution, require offline processing in most cases, and exhibit limited robustness in complex scenes. With the development of deep learning, the end-to-end, data-driven paradigm has gradually become dominant. StabNet [48] was the first to propose a supervised online stabilization framework based on convolutional neural networks (CNNs), followed by PW-StableNet [60] and Yu et al. [56], which introduced pixel-level 2D deformation fields for more precise motion correction. FuSta [30] improved stabilization performance by integrating multi-scale spatial and feature information, while DIFRINT [7] effectively reduced cropping artifacts through unsupervised inter-frame interpolation. Subsequently, DUT [52] achieved stabilization without manual annotation by utilizing motion priors or trajectory consistency. NNDVS [58] achieved high-quality, low-latency video stabilization using existing motion estimation frameworks. FastStab [61] enabled fast offline 2D stabilization through optical flow guidance. To further enhance temporal consistency and scene adaptability, VidStabFormer [21] and MetaStab [1] introduced self-supervised and meta-learning strategies, respectively. In recent years, 3D-based stabilization techniques have emerged: Deep3D [23] jointly estimates depth and pose; DeepFused [40] integrates optical flow and gyroscope data to predict virtual 3D camera trajectories; RStab [34] employs a neural rendering technique with adaptive modules; and Gavs [54] achieves high-fidelity, clipping-free stabilization through Gaussian-based 3D scene reconstruction. Despite these advances, deep learning methods are often complex and resource-intensive. As an efficient alternative, our method adopts a hybrid strategy that integrates multi-threaded buffering technology into a three-stage processing pipeline.

### 2.2. Feature Detection

Classical detectors [31, 36, 37] remain widely used, whereas deep methods [8, 11, 35, 38, 45, 62, 63] have been shown to improve robustness to illumination and viewpoint changes. In addition, methods [42, 50] have achieved strong performance in low-texture and large-parallax cases. Existing stabilizers often rigidly couple detection, limiting adaptability. We propose a decoupled framework with keypoint uniformization and multi-detector collaboration, enabling scene-adaptive feature selection while retaining real-time efficiency.

### 2.3. Optical Flow Estimation

Variational methods [15] pioneered the use of global optimization, while deep methods such as those in [10, 16–19, 39, 41, 43] achieved state-of-the-art accuracy. NeuFlow [59] targets edge devices. For stabilization, optical flow can aggregate local motion cues into global priors. MemFlow [9] demonstrated real-time performance by incorporating historical memory. Optical flow better captures non-rigid motion than top-down keypoint matching.

## 3. Method

Our pipeline consists of three stages: (i) motion estimation, (ii) motion propagation, and (iii) motion compensation. All three stages are strictly causal (i.e., past-only) and never access future frames. Training is fully unsupervised (see the self-supervised objectives in Secs. 3.2 and 3.3); inference utilizes a multi-threaded, asynchronous pipeline for enhanced efficiency. Due to space constraints, full details of our multi-process acceleration strategy are deferred to the supplementary material (Sec. C).

### 3.1. Motion Estimation

This section presents a strictly online observation pipeline that outputs keypoints  $K_t$ , displacements  $\mathbf{u}_t$ , and a causal dense backward flow  $\hat{\mathbf{f}}_{t \leftarrow t-1}$ . These serve as inputs to motion propagation and motion compensation. This step depends only on  $\{I_{t-1}, I_t\}$  and never uses future frames.

**Notation** Let  $I_t$  represent the  $t$ -th frame. We generate online: (i) candidate keypoints  $\tilde{K}_t = \{(x_i, y_i, s_i)\}_i$  (with confidence  $s_i$ ); (ii) the uniformized subset  $K_t$ ; and (iii) a causal dense backward optical flow  $\hat{\mathbf{f}}_{t \leftarrow t-1} \in \mathbb{R}^{H \times W \times 2}$ , estimated from  $\{I_{t-1}, I_t\}$ . Next, we sample the observed displacements  $\mathbf{u}_t$  at the keypoint locations and construct the feature representation for subsequent modules.

**(1) Keypoint Collaboration Detection** To reduce the computational cost and mitigate dynamic-object sensitivity in dense flow methods [2, 55], we adopt a flexible framework that incorporates feature points from heterogeneous detectors. Let

$$\mathcal{D} = \{D_m^{\text{trad}}\}_{m=1}^M \cup \{D_n^{\text{deep}}\}_{n=1}^N, \quad (1)$$

with each producing  $\tilde{K}_t^{(j)} = \{(x_i, y_i, s_i)^{(j)}\}_i$ . We normalize the confidence scores, apply NMS, and fuse the proposals from different sources using weighted averages:

$$\tilde{K}_t = \text{NMS}\left(\bigcup_j w_j \cdot \tilde{K}_t^{(j)}\right), \quad (2)$$

where  $w_j$  can be configured online according to scene characteristics or runtime budget.

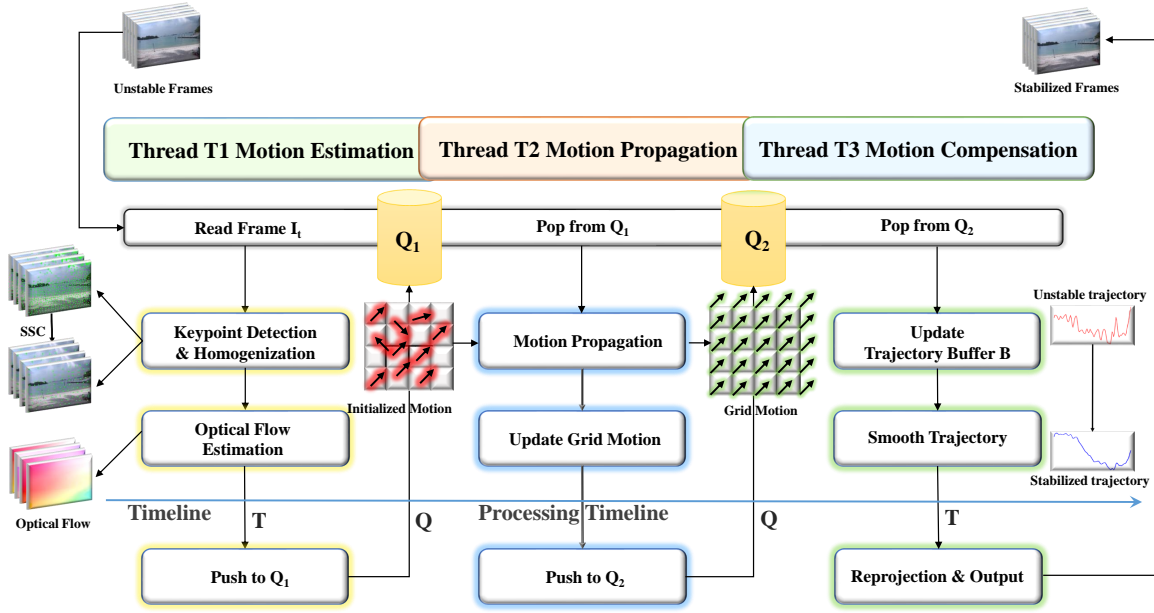


Figure 2. Overview of our video stabilization framework, consisting of three key modules: motion estimation, motion propagation, and motion compensation. The motion estimation module detects keypoints and calculates optical flow to estimate motion between frames. The motion propagation module transfers the estimated motion information to a global trajectory buffer, ensuring motion consistency across frames. The motion compensation module adjusts the frames based on the updated trajectories to produce a stabilized output. A multi-threaded processing structure utilizes three threads, each dedicated to one of the core modules, and leverages shared buffer queues for efficient parallel execution. This approach improves processing speed and online performance, enabling the stabilization of video frames with minimal latency.

(2) **Homogenization** To prevent clustering of keypoints in texture-rich regions, we employ Spatially Selective Clustering (SSC) [3]. The image is partitioned into a  $G_x \times G_y$  grid; for each cell  $\mathcal{C}$ , the top- $k$  keypoints are selected based on confidence  $s$ , subject to a minimum separation threshold  $\tau$ :

$$K_t = \bigcup_c \arg \operatorname{top}_k \left\{ (x, y, s) \in \tilde{K}_t \cap \mathcal{C} \mid \min_{(x', y') \in \tilde{K}_t \cap \mathcal{C}} \|(x, y) - (x', y')\|_2 \geq \tau \right\}. \quad (3)$$

(3) **Sparse Keypoint-Guided Causal Flow Fusion** We estimate the causal dense backward flow  $\mathbf{f}_{t \leftarrow t-1}$  using MemFlow [9]. To incorporate guidance from sparse keypoints, we build the mask using the denser candidate set  $\tilde{K}_t$  (to improve coverage), while the uniformized subset  $K_t$  is used for subsequent geometric estimation.

$$M_t(x) = \mathbf{1} \left[ \min_{p \in \tilde{K}_t} \|x - p\|_2 \leq r \right]. \quad (4)$$

where the mask is set to 1 within a circular neighborhood of radius  $r$  centered at each keypoint, and 0 elsewhere.

We then synthesize a reweighted flow field by directly using the estimated dense flow within the keypoint neighborhood, while using keypoint-based interpolated flow outside the neighborhood:

$$\hat{\mathbf{f}}_{t \leftarrow t-1}(x) = M_t(x) \odot \mathbf{f}_{t \leftarrow t-1}(x) + (1 - M_t(x)) \odot \mathcal{I}(\mathbf{f}_{t \leftarrow t-1}, \tilde{K}_t), \quad (5)$$

Finally, we extract the optical flow displacements at the keypoint locations from the reweighted flow field  $\hat{\mathbf{f}}_{t \leftarrow t-1}$  as the observation:

$$\mathbf{u}_t = \hat{\mathbf{f}}_{t \leftarrow t-1}(K_t) \in \mathbb{R}^{|K_t| \times 2}, \quad (6)$$

and concatenate them with the keypoint coordinates to form the motion feature vector for subsequent tasks:

$$\mathbf{m}_t = [x_{kp}; y_{kp}; u; v]. \quad (7)$$

### 3.2. Motion Propagation

While sparse keypoints and their associated initialized flow can capture local motion, dynamic and non-rigid scenes still pose challenges to modeling the camera's global trajectory. To address this, we propose **EfficientMotionPro**,

which anchors displacements to a regular grid using multi-homography priors, while focusing on learning only the non-rigid/parallax residuals. This design produces a full-frame grid motion field  $\Delta g_t$ . Importantly, both training and inference rely solely on past information (without access to future frames), and the entire process is conducted in a fully self-supervised manner. We denote the set of *causal keypoints* at time  $t$  as  $\Omega_{kp}$  and the set of grid vertices as  $\Omega_{grid}$ .

**(1) Multi-Grid Homography Prior** Let  $K_{\text{homo}} \geq 1$  be a hyperparameter (the number of homography clusters). We cluster  $\mathbf{u}_t$  into  $K_{\text{homo}}$  groups via K-means and estimate a homography for each cluster with RANSAC, yielding  $H_{t,1}, \dots, H_{t,K_{\text{homo}}}$ . Let  $g$  denote the regular grid vertices ( $g \in \Omega_{grid}$ ); projecting  $g$  produces  $\{\hat{g}_{t,k}\}_{k=1}^{K_{\text{homo}}}$ . We then compute soft fusion weights  $\{\alpha_{t,k}(g)\}_{k=1}^{K_{\text{homo}}}$  based on local cluster prevalence or distance, with  $\sum_k \alpha_{t,k}(g) = 1$ :

$$\hat{g}_t = \sum_{k=1}^{K_{\text{homo}}} \alpha_{t,k}(g) \hat{g}_{t,k}, \quad \Delta g_{\text{base},t} = g - \hat{g}_t. \quad (8)$$

**(2) Residual Network** Given  $\mathbf{m}_t = [x_{kp}; y_{kp}; u; v]$ , a lightweight backbone (Ghost [14]+ECA [49]) predicts per-vertex residuals  $\Delta g_{\text{res},t}$ , from which we obtain

$$\Delta g_t = \Delta g_{\text{base},t} + \Delta g_{\text{res},t}. \quad (9)$$

All temporal operators are implemented as causal convolutions (left-padded).

**(3) Core Self-Supervised Loss** Our unsupervised objective enforces that the predicted grid displacements remain consistent with the observed causal keypoint motions. To improve robustness against noise and outliers, we adopt the Charbonnier penalty [5] and further introduce per-keypoint confidence weights  $\omega_{t,p} \in [0, 1]$  that adaptively down-weight unreliable keypoints:

$$\mathcal{L}_{\text{kp}} = \frac{1}{|\Omega_{kp}|} \sum_{p \in \Omega_{kp}} \omega_{t,p} \sqrt{\|\mathbf{u}_{t,p} - \Delta g_t(p)\|_2^2 + \epsilon^2}, \quad (10)$$

where  $\epsilon$  is a small stabilizing constant (e.g.,  $10^{-3}$ ).

This confidence-weighted keypoint consistency loss serves as the core driver of propagation. Additional regularization terms (e.g., projection consistency and a structure-preservation constraint) are incorporated to further improve stability and prevent degenerate solutions; see supplement (Sec. A).

### 3.3. Motion Compensation

In dynamic scenes or under low-frame-rate conditions, grid vertex trajectories often exhibit local oscillations due to jitter, occlusion, or non-rigid disturbances, which compromise the stability of the overall motion field. To mitigate this issue, we introduce **OnlineSmoother**, a lightweight online trajectory smoothing module inspired by [47, 58]. Without relying on future frames, it employs a learnable causal kernel to smooth propagation-generated trajectories, followed by frame-wise grid deformation that produces stabilized videos. Neither training nor inference requires annotations or ground-truth data.

**(1) Causal Kernel Smoother** A left-padded causal convolution encodes long-term memory; the decoder predicts 3-tap causal kernels for the  $x$  and  $y$  directions (6 channels total), corresponding to an effective temporal window of  $L=7$  frames. We denote the kernel tensor by

$$\mathcal{K} = \text{concat}(\mathcal{K}^x, \mathcal{K}^y) \in \mathbb{R}^{B \times 6 \times T \times H \times W}, \quad (11)$$

where  $B$  is the batchsize,  $T$  is the number of causal time steps held in the buffer, and  $H \times W$  is the grid resolution (number of vertices in  $\Omega_{grid}$ ). For the  $x$  direction at time  $t$ ,

$$S_t^x = \frac{\lambda \sum_{r \in \{1,2,3\}} k_{t,r}^x S_{t-r}^x + O_t^x}{1 + \lambda \sum_r |k_{t,r}^x|}, \quad (12)$$

where  $O_t$  is the input trajectory (e.g., grid-vertex trajectories from  $\Delta g_t$  or its integral) and  $\lambda=100$  by default. Only cached past states are accessed (no look-ahead). We empirically set  $L=7$  and use  $\Delta_{\text{max}} = \lfloor (L-1)/2 \rfloor = 3$  in the temporal loss below; see figure 5 for ablations.

**(2) Core Self-Supervised Loss (definitions included)** To ensure stable yet responsive trajectories under causal constraints, we combine a time-adaptive second-order penalty with a frequency prior. Let  $p \in \Omega_{grid}$  index grid vertices. The adaptive temporal term is

$$\mathcal{L}_{\text{time}} = \frac{1}{|\Omega_{grid}|} \sum_{p \in \Omega_{grid}} \sum_{\Delta=1}^{\Delta_{\text{max}}} \frac{\alpha_{\Delta} e^{-\beta \|S_t(p) - S_{t-\Delta}(p)\|_2^2}}{\Delta^2} \cdot \sqrt{\|S_t(p) - 2S_{t-\Delta}(p) + S_{t-2\Delta}(p)\|_2^2 + \epsilon^2}. \quad (13)$$

**Definitions.** (i)  $\Delta_{\text{max}} \in \mathbb{N}$  is the causal horizon used by the loss (we set  $\Delta_{\text{max}}=3$  for  $L=7$  so that the largest stencil  $t - 2\Delta$  remains within the causal window). (ii)  $\alpha_{\Delta} \geq 0$  are fixed, distance-decaying weights

$$\alpha_{\Delta} = \frac{\exp(-\Delta/\tau_{\text{time}})}{\sum_{d=1}^{\Delta_{\text{max}}} \exp(-d/\tau_{\text{time}})}, \quad (14)$$

where  $\tau_{\text{time}} = 2$  by default.

(iii)  $\beta \geq 0$  controls motion-adaptive attenuation; we use a global *learnable* scalar with softplus reparameterization, initialized to  $\beta_0=0.02$ . Larger  $\beta$  downweights the penalty when recent motion magnitude  $\|S_t - S_{t-\Delta}\|$  is large.

The frequency term suppresses high-frequency oscillations within each causal window of length  $L$ :

$$\mathcal{L}_{\text{freq}} = \frac{1}{|\Omega_{\text{grid}}|} \sum_{p \in \Omega_{\text{grid}}} \sum_{m=1}^{\lfloor L/2 \rfloor} \gamma(\omega_m) \|\hat{S}_p(\omega_m)\|_2^2, \quad (15)$$

where  $\hat{S}_p(\omega_m)$  is the DFT magnitude of  $\{S_{t-d}(p)\}_{d=0}^{L-1}$  at frequency  $\omega_m = 2\pi m/L$ , and the frequency weights are  $\gamma(\omega_m) = \gamma_0 \left(\frac{\omega_m}{\omega_N}\right)^2$  with  $\omega_N = \pi$  and  $\gamma_0 \geq 0$ , by default we set  $\gamma_0 = 0.1$ .

The overall temporal objective is

$$\mathcal{L}_{\text{temp}} = \lambda_{\text{time}} \mathcal{L}_{\text{time}} + \lambda_{\text{freq}} \mathcal{L}_{\text{freq}}, \quad (16)$$

with  $\lambda_{\text{time}}, \lambda_{\text{freq}} > 0$  (default  $\lambda_{\text{time}} = 1.0, \lambda_{\text{freq}} = 0.1$ ). All loss terms are fully causal.

**(3) Frame-Level Compensation and Rendering** Let  $M_t = S_t - O_t$  denote the compensation displacement field (defined on grid vertices). For each pixel  $x$ , obtain  $M_t(x)$  by bilinear interpolation from vertex displacements, and perform either forward grid warping or backward sampling:

$$x' = x + M_t(x), \quad \tilde{I}_t(x) = I_t(\mathcal{W}(x; M_t)). \quad (17)$$

where  $\mathcal{W}$  is the backward mapping with bilinear resampling to avoid holes. We employ ProPainter [64] for outpainting at frame boundaries to minimize black borders; see supplement (Sec. D) for details.

### 3.4. UAV-Test Dataset

Most existing video stabilization benchmarks are collected with handheld devices under visible-light conditions, which limits their applicability in real-world scenarios. In contrast, unstable videos frequently arise in safety-critical domains such as UAV-based night-time remote sensing and guided munitions. To bridge this gap, we introduce the **UAV-Test** dataset, comprising unstable aerial videos in both visible and infrared modalities. **UAV-Test** contains 92 sequences spanning five representative scenarios: urban areas, highways, forests/mountains, waterfronts, and industrial sites. Summary statistics are reported in Table 1, with additional implementation details and extended dataset analysis provided in the supplemental material (Sec. E).

## 4. Experiment

### 4.1. Quantitative Evaluation

**Baselines.** We evaluate our method against a diverse set of representative stabilization algorithms, covering both of-

fline and online approaches. Offline baselines include [1, 7, 13, 21, 23, 26, 30, 34, 52, 54, 56, 60] together with the commercial stabilizer *Adobe Premiere Pro 2025*. Online methods include [28, 29, 48, 58]. For comparison, we use either official videos or results from official implementations with default settings or pretrained models.

**Datasets.** We evaluate on three public benchmarks and an additional multimodal UAV dataset: (1) *NUS* [26], 144 sequences across six categories (Regular, Running, Zooming, Crowd, Parallax, QuickRotating); (2) *DeepStab* [48], 60 pairs of synchronized unstable/stable videos; (3) *Selfie* [57], 33 front camera sequences with severe shaking; (4) *GyRo* [40], which consists of 50 videos with precise alignment of gyroscope and OIS data; the test set is divided into six categories: GENERAL, ROTATION, PARALLAX, DRIVING, PEOPLE, and RUNNING; (5) *UAV-Test*, consisting of 92 videos (74 RGB, 18 infrared) captured by UAVs across diverse scenarios, including urban highways, forests, dense cities, industrial sites, and waterfronts.

**Metrics.** Following prior works [23, 30, 34, 48, 52, 58], we report three metrics: (1) *Cropping Ratio (C)*: content preservation after stabilization (higher is better); (2) *Distortion Value (D)*: anisotropy of estimated homographies, indicating geometric fidelity (higher is better); (3) *Stability Score (S)*: low-frequency energy ratio, reflecting motion smoothness (higher is better). Together, these metrics capture content integrity, geometric fidelity, and temporal stability.

**Results on the NUS dataset.** On the NUS benchmark [26] (Table 2), our method achieves the best online performance across all three metrics ( $C = 0.95, D = 0.98, S = 0.90$ ). Compared with NNDVS [58], our approach matches its geometric fidelity ( $D = 0.98$ ) while surpassing it in stability and cropping. This highlights our advantage in maintaining boundary completeness and suppressing distortion, while remaining close to the strongest offline method RStab [34].

**Results on the DeepStab dataset.** For DeepStab [48] (paired 720p), our method ranks first among online methods in Cropping Ratio ( $C = 0.94$ ), ties with NNDVS in geometric fidelity ( $D = 0.91$ ), and achieves competitive stability ( $S = 0.85$ , second only to MeshFlow [28] at 0.86). This shows good transfer from low resolution, fast shaking scenarios to higher definition inputs, achieving a balanced trade-off between smoothness and content preservation.

**Results on the Selfie dataset.** The Selfie dataset [57], with severe handheld shake and large motion, poses challenges to stabilization. As reported in Table 2 (center right), our method delivers the best online performance with  $C = 0.98, D = 0.93$ , and  $S = 0.91$ . This confirms that our model handles extreme motion and dynamic scenes better than traditional geometric and deep content-driven baselines.

**Results on the GyRo dataset.** On the GyRo benchmark [40], which involves gyroscope-based scenarios, our

Table 1. Overview of the UAV-Test dataset.

Scene Type	Sensor	Tilt Range	Resolution	FPS	Occlusion	Sequences
Urban areas	Visible/IR	30°- 90°	1920 × 1080	25	Partial building occlusion	19
Highways	Visible/IR	30°- 90°	1280 × 720	30	Minimal occlusion	22
Forests/mountains	Visible/IR	45°- 90°	1920 × 1080	25	Frequent canopy occlusion	18
Waterfronts	Visible	60°- 90°	1920 × 1080	30	Mild vapor occlusion	20
Industrial sites	Visible/IR	30°- 60°	1280 × 720	25	Large machinery occlusion	13

Table 2. Quantitative results on the NUS [26], DeepStab [48], Selfie [57], GyRo [40] and UAV-Test datasets. We report Cropping Ratio (C), Distortion Value (D), and Stability Score (S). All metrics range from 0 to 1; higher is better. Best results in each group (offline or online) are in red, second best in blue. A runtime (fps) comparison among online methods is provided in the supplementary material (Sec. F).

Method	NUS			DeepStab			Selfie			GyRo			UAV-Test			
	C↑	D↑	S↑	C↑	D↑	S↑	C↑	D↑	S↑	C↑	D↑	S↑	C↑	D↑	S↑	
Offline	Grundmann et al. [13]	0.71	0.76	0.82	0.77	0.87	0.84	0.75	0.81	0.83	0.91	0.89	0.81	0.72	0.64	0.76
	Bundle [26]	0.81	0.78	0.82	0.80	0.90	0.85	0.74	0.82	0.80	0.93	0.82	0.85	0.79	0.69	0.88
	DIFRINT [7]	1.00	0.87	0.84	1.00	0.91	0.78	1.00	0.78	0.84	1.00	0.83	0.85	1.00	0.86	0.87
	Yu and Ramamoorthi [56]	0.85	0.81	0.86	0.87	0.92	0.82	0.83	0.79	0.86	1.00	0.92	0.84	0.85	0.83	0.86
	PWStableNet [60]	0.91	0.97	0.86	0.97	0.97	0.87	0.99	0.92	0.89	0.99	0.96	0.83	0.90	0.88	0.90
	DUT [52]	0.98	0.88	0.85	0.99	0.95	0.95	0.99	0.98	0.93	0.99	0.98	0.89	0.95	0.89	0.94
	Deep3D [23]	0.66	0.90	0.94	0.75	0.98	0.92	0.35	0.70	0.95	0.99	0.94	0.77	0.68	0.89	0.86
	FuSta [30]	1.00	0.87	0.86	1.00	0.83	0.87	1.00	0.92	0.82	1.00	0.97	0.87	1.00	0.88	0.83
	RStab [34]	1.00	0.99	0.94	1.00	0.98	0.96	1.00	0.92	0.95	1.00	0.95	0.92	1.00	0.96	0.94
	MetaStab [1]	1.00	0.99	0.91	1.00	0.99	0.91	1.00	0.96	0.58	1.00	0.99	0.90	1.00	0.99	0.91
	VidStabFormer [21]	1.00	0.90	0.85	1.00	0.90	0.82	1.00	0.85	0.88	1.00	0.89	0.86	1.00	0.87	0.84
	Gavs [54]	1.00	0.98	0.93	1.00	0.96	0.90	1.00	0.78	0.85	1.00	0.99	0.93	1.00	0.83	0.87
Adobe Premiere Pro (2025)	0.84	0.82	0.91	0.73	0.87	0.87	0.71	0.80	0.84	0.73	0.96	0.60	0.75	0.86	0.90	
Online	MeshFlow [28]	0.78	0.83	0.85	0.81	0.87	0.86	0.75	0.88	0.84	0.79	0.88	0.82	0.77	0.83	0.70
	StabNet [48]	0.66	0.88	0.82	0.65	0.86	0.80	0.70	0.78	0.83	0.69	0.85	0.83	0.73	0.84	0.73
	NNDVS [58]	0.92	0.98	0.87	0.93	0.91	0.84	0.97	0.92	0.91	0.99	0.93	0.88	0.89	0.87	0.84
	Liu et al. [29]	0.72	0.89	0.89	0.89	0.88	0.85	0.79	0.89	0.85	0.99	0.94	0.89	0.82	0.89	0.85
	Ours	0.95	0.98	0.90	0.94	0.91	0.85	0.98	0.93	0.91	0.99	0.96	0.93	0.94	0.90	0.89

method achieves state-of-the-art online performance with Cropping Ratio ( $C = 0.99$ ), Distortion Value ( $D = 0.96$ ), and Stability Score ( $S = 0.93$ ). This outperforms other online approaches, such as NNDVS [58] ( $C = 0.99$ ,  $D = 0.93$ ,  $S = 0.88$ ) and Liu et al. [29] ( $C = 0.99$ ,  $D = 0.94$ ,  $S = 0.89$ ), and is competitive with top offline methods like Gavs [54] ( $C = 1.00$ ,  $D = 0.99$ ,  $S = 0.93$ ), demonstrating the effectiveness of our causal framework.

**Results on the UAV-Test dataset.** Finally, on the new UAV-Test benchmark with visible/IR sequences across diverse scenarios, our method sets a new online state of the art:  $C = 0.94$ ,  $D = 0.90$ ,  $S = 0.89$ , outperforming NNDVS [58] ( $C = 0.89$ ,  $D = 0.87$ ,  $S = 0.84$ ) and Liu et al. [29] ( $C = 0.82$ ,  $D = 0.89$ ,  $S = 0.85$ ). Compared with the strongest offline models (e.g., RStab [34]), our results remain competitive while relying only on causal information, showcasing strong generalization across modalities

and complex UAV scenarios.

## 4.2. Qualitative Results

The visual comparison results in Figure 3 show that competing online methods [28, 29, 48, 58] often produce artifacts such as shear, distortion, or excessive cropping. In contrast, our method generates fewer artifacts across various scenes and is more effective at preserving scene structure, demonstrating superior generalization without the use of future frames.

## 4.3. User Study

We conducted a user study to compare our method with other online approaches [28, 29, 48, 58]. Five datasets were prepared, each containing two randomly selected video types. Fifty participants ranked the videos from best to worst based on their preference. The videos were randomly

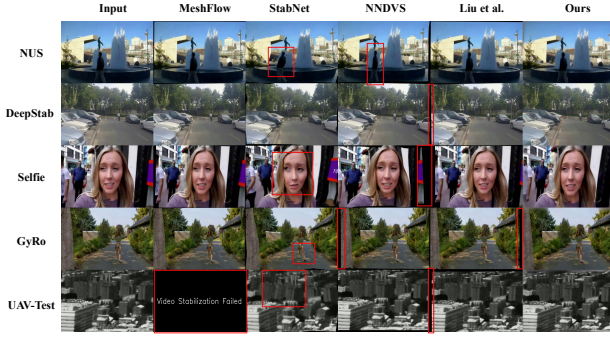


Figure 3. Comparison of visual results across different online methods. Distorted regions and black borders are highlighted with red boxes.

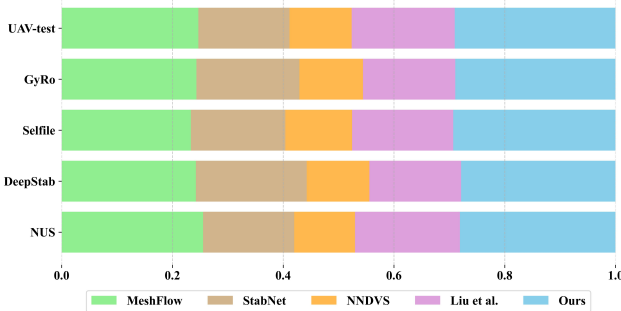


Figure 4. User study preferences.

ordered and included the original unstable videos. The results, shown in Figure 4, indicate that users generally preferred our videos as the best. See the supplemental material (Sec. I) for details.

## 5. Ablation Study

We perform ablation experiments on multiple datasets, as shown in Fig. 5, where A10 is the full model ( $L = 7$ ). The results demonstrate the effectiveness of each component:

- **w/o MP (Sec. 3.2):** Removing motion propagation (A1) degrades D and PSNR, confirming its importance for global motion modeling.
- **w/o TS (Sec. 3.3):** Without trajectory smoothing (A2), structural stability decreases, as reflected in higher D.
- **w/o MP&TS:** Disabling both (A3) causes the most severe drop, highlighting their complementarity.
- **w/o  $Loss_{kp}$  (Eq. 10):** Excluding keypoint consistency loss (A4) weakens motion supervision, lowering D and slightly PSNR.
- **w/o  $Loss_{temp}$  (Eq. 16):** Without temporal regularization (A5), grid trajectories become less stable, increasing D while PSNR remains similar.
- **w/o Homo (Sec. 3.2):** Replacing multi-homography with

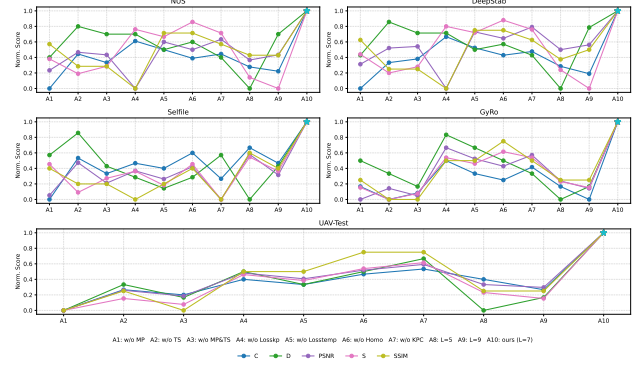


Figure 5. Normalized ablation study results on five datasets (NUS, DeepStab, Selfie, GyRo, UAV-Test). The x-axis denotes ablation configurations A1–A9 (variants with modules removed/modified) and A10 (our full model with window length  $L = 7$ ). The y-axis shows normalized scores (higher is better) for five metrics: Consistency (C), Distortion Value (D), Peak Signal-to-Noise Ratio (PSNR), Stability Score (S), and Structural Similarity (SSIM).

a single homography (A6) introduces jitter and local distortions, reducing D and SSIM.

- **w/o KPC (Sec. 3.1):** Using raw keypoints without collaboration (A7) leads to uneven sampling and lower D.
- **Window length (Sec. 3.3):** Shorter windows (A8,  $L = 5$ ) improve stability but reduce fidelity, while longer windows (A9,  $L = 9$ ) increase cost without consistent gains.  $L = 7$  (A10) provides the best trade-off.

Overall, the full model achieves the highest scores, validating the contribution of each module.

## 6. Conclusion

In this paper, we present a novel, lightweight, unsupervised framework for online video stabilization that overcomes the limitations of conventional end-to-end models, namely strong reliance on paired datasets, limited controllability, and difficulty of deployment on resource-constrained devices. The framework comprises three stages: motion estimation, motion propagation, and motion compensation, together with a system-level multithreaded acceleration strategy. By introducing collaborative keypoint detection and a keypoint uniformization scheme, the framework achieves accurate and robust motion estimation. Coupled with grid-based residual propagation and a dynamic smoothing kernel generation mechanism, it enables fine-grained modeling of complex motion trajectories with online smoothing. A multithreaded buffering mechanism further ensures stable operation on embedded platforms. In addition, we introduce a new multimodal aerial view dataset of unstable videos, UAV-Test, covering diverse geographic scenes and viewpoints to complement existing benchmarks. Extensive experiments show that our method outperforms state-of-the-

art online approaches overall and approaches the performance of offline methods, demonstrating strong potential for real-time applications.

## 7. Appendix

The supplementary material additionally provides the following:

- Implementation details of the motion propagation networks;
- Implementation details of the trajectory smoothing networks;
- Details of the multi-threaded asynchronous buffering pipeline;
- Details of frame outpainting;
- Information on the multimodal UAV dataset;
- Runtime comparison on embedded platforms;
- Comprehensive description of the evaluation metrics used in this work;
- Per-scene quantitative evaluation of online methods;
- Additional visualizations of key modules and optical flow;
- A 3-minute video demonstrating comparisons with online methods;
- Limitations and future directions.

## 8. Details of EfficientMotionPro

### 8.1. Training Objectives

We propose a grid-based motion propagation network (**EfficientMotionPro**). Building upon multi-homography priors, this module explicitly encodes the relationship between sparse keypoint residuals and vertex distances. Through lightweight feature extraction, attention-weighted aggregation, and residual decoding, it achieves end-to-end propagation from sparse keypoints to a dense grid, thereby yielding a more robust global motion field. We additionally employ projection consistency and structure-preservation objectives for training.

**(1) Homography Projection Constraint** To enhance the geometric fidelity of the propagated motion field, we introduce a homography-based projection loss. Specifically, the estimated keypoint motion is projected via a local homography mapping generated from the predicted grid motion vectors. The Euclidean distance between this projected position and the actual ground-truth keypoint position after motion constitutes the projection error:

$$\mathcal{L}_{\text{proj}} = \frac{1}{|\Omega_{k_p}|} \sum_{p \in \Omega_{k_p}} \omega_{t,p} \sqrt{\|\mathbf{u}_{t,p} - H_t^{\text{local}}(p; \Delta g_t) \cdot p\|_2^2 + \epsilon^2}. \quad (18)$$

Here,  $H_t^{\text{local}}(p; \Delta g_t)$  denotes the local homography transformation, obtained via bilinear sampling from the grid mo-

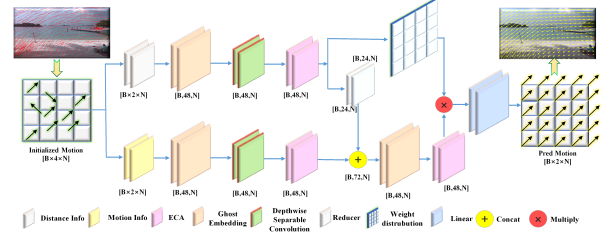


Figure 6. The architecture of our EfficientMotionPro network.

tion field  $\Delta g_t$  surrounding point  $p$ . This term effectively constrains the grid deformation predicted by the residual network to be geometrically plausible, reducing inconsistent distortions.

**(2) Structure-Preservation Constraint** In low-texture regions, the propagation estimate is prone to local distortions or discontinuous boundaries. To maintain the rigid structure of the mesh, we design a structure-preserving loss based on the angular relationships between adjacent vertices. For each grid cell defined by its four vertices  $\{g_{i,j}, g_{i+1,j}, g_{i,j+1}, g_{i+1,j+1}\}$ , we enforce orthogonality between adjacent edges:

$$\mathcal{L}_{\text{struct}} = \frac{1}{|G|} \sum_{i,j} \left( \frac{\langle g_{i+1,j} - g_{i,j}, R_{90^\circ}(g_{i,j+1} - g_{i,j}) \rangle}{\|g_{i+1,j} - g_{i,j}\| \cdot \|g_{i,j+1} - g_{i,j}\|} \right)^2, \quad (19)$$

where  $R_{90^\circ}$  denotes a  $90^\circ$  rotation operator,  $\langle \cdot, \cdot \rangle$  is the dot product, and  $|G|$  is the total number of grid cells. This loss penalizes deviations from orthogonality, suppressing shear and anisotropic scaling, thereby preserving local shape and preventing distortion.

**(3) Total Loss** The final optimization objective for the motion-propagation module is defined as the weighted combination of all three losses:

$$\mathcal{L} = \lambda_1 \mathcal{L}_{\text{kp}} + \lambda_2 \mathcal{L}_{\text{proj}} + \lambda_3 \mathcal{L}_{\text{struct}}, \quad (20)$$

with default settings  $(\lambda_1, \lambda_2, \lambda_3) = (10, 40, 40)$ .

### 8.2. Network Architecture

Fig. 6 illustrates the architecture of our EfficientMotionPro network. Each frame produces an input tensor of size  $[B, 4, N]$  constructed from  $N$  keypoints: two channels encode distance (or distance-derived) features and two channels encode residual motion. Distance and motion branches use Ghost [14] modules for lightweight embeddings and depthwise separable convolutions; motion features are refined with ECA [49] attention. Features are fused via a Lightweight Fusion Block, aggregated with attention weights, and decoded by a two-layer MLP to yield

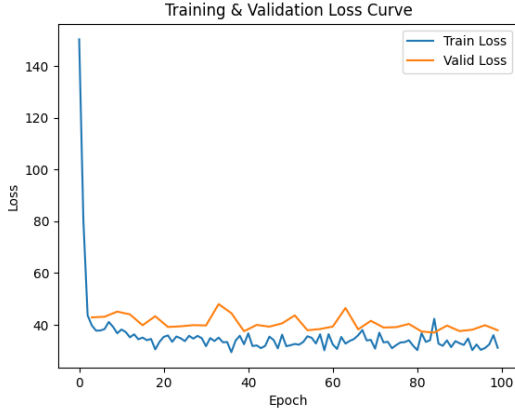


Figure 7. Training curves of **EfficientMotionPro**: the blue line shows training loss and the orange line shows validation loss.

residuals  $[B, 2]$ . The final displacements are reshaped into a grid field  $[H/P, W/P, 2]$  and smoothed by median pooling. Table 3 details the configuration.

**(1) Implementation Details** We train **EfficientMotionPro** on an in-house unstable video dataset [20, 65, 66] with train/val splits. Batch size is 64; optimizer is Adam ( $\beta_1 = 0.9, \beta_2 = 0.999$ ) with weight decay  $1 \times 10^{-5}$ . Learning rate follows OneCycleLR, peaking at  $2 \times 10^{-4}$  with 30% warm-up, then cosine decay. Training is conducted for 100 epochs on a single NVIDIA RTX 4090 GPU, taking approximately 12 hours. We save checkpoints every 3 epochs and keep the best validation loss as shown in Fig. 7.

## (2) Complexity Analysis

**Parameter Count** Let  $C_e$  be the embedding dimension (default  $C_e = 48$ ). Core components include Ghost modules, depthwise separable convolutions (DW), pointwise convolutions (PW, kernel 1), and ECA attention. At  $C_e = 48$ , the whole module has  $\sim 2.3 \times 10^4$  ( $\approx 22.9$ K) parameters, significantly fewer than those in typical full-frame 2D CNN or Transformer-based propagation heads.

**Time Complexity** Let  $N$  be the number of keypoints per frame. Since convolutions, softmax, and weighted aggregation are along the keypoint dimension with small kernels, the dominant MACs come from PW convolutions:

$$\begin{aligned}
 & \mathcal{O}(NC_e^2) \text{ [PW: dist reduction } C_e \rightarrow C_e/2] \\
 & + \mathcal{O}(4NC_e^2) \text{ [PW: motion } 2C_e \rightarrow 2C_e] \\
 & + \mathcal{O}(NC_e^2) \text{ [PW: motion } C_e \rightarrow C_e] \\
 & + \mathcal{O}(NC_e k) \text{ [DW blocks]} + \mathcal{O}(N) \text{ [aggregation]} \\
 & \approx \mathcal{O}(5NC_e^2).
 \end{aligned} \tag{21}$$

Thus the cost scales linearly with  $N$  and is largely decoupled from image resolution or grid size; the cost of median pooling is negligible due to its small kernel size.

**Memory Complexity** Intermediate tensors scale as  $\mathcal{O}(BC_e N)$  (independent of  $HW$ ).

**Complexity Estimation** Numerical MAC estimates (ignoring BN/activations/ECA) with  $C_e = 48$  are shown in Table 4.

## 9. OnlineSmoother Details

### 9.1. Training Objectives

In dynamic scenes or under low-frame-rate conditions, grid vertex trajectories often exhibit local oscillations due to jitter, occlusion, or non-rigid disturbances, which compromise temporal consistency and introduce geometric distortions. To achieve online stabilization with minimal latency and without using future frames, we introduce the **OnlineSmoother** network. It leverages only the historical trajectory data from a sliding buffer, employing a Lite LS-3D [46] encoder to extract spatio-temporal features and a Star-gated [32] decoder to predict dynamic smoothing kernels for the  $x$  and  $y$  directions separately. This kernel-based iterative update mechanism progressively suppresses high-frequency oscillations while preserving motion intentionality. We additionally employ spatial consistency and projection consistency objectives for training.

**(1) Spatial Distortion Constraint** To maintain the local geometric structure of the mesh during temporal transformation, we introduce a distortion loss based on triangular mesh elements. The smoothed trajectories are mapped back to the grid coordinate system to construct triangular structures (eight varying configurations per quad). The loss penalizes deviations in edge length ratios and angles from their initial reference state:

$$\begin{aligned}
 \mathcal{L}_{\text{spatial}} = \frac{1}{|G|} \sum_{i,j} & \left[ \lambda_{\text{edge}} \sum_{\text{edges } e} \sqrt{\left( \frac{\|e\|}{\|e_0\|} - 1 \right)^2 + \epsilon^2} \right. \\
 & \left. + \lambda_{\text{angle}} \sum_{\text{angles } \theta} \sqrt{\left( \frac{\theta}{\theta_0} - 1 \right)^2 + \epsilon^2} \right]
 \end{aligned} \tag{22}$$

where  $e_0$  and  $\theta_0$  represent the edge lengths and angles of the triangles in the initial, undeformed reference mesh  $g_{\text{ref}}$ , and  $|G|$  is the total number of grid cells.

**(2) Keypoint Projection Consistency Constraint** To further ensure the alignment between the smoothed motion field and the observed keypoint trajectories, we introduce

Table 3. Architecture of the proposed **EfficientMotionPro** module. The input tensor  $[B, 4, N]$  is split into distance and motion channels, embedded via Ghost modules, enhanced with ECA, fused, and finally decoded into grid displacements.

Component	Operation	Output Size
Input	Distance & Motion channels	$[B, 4, N]$
Distance branch	GhostModule + DWConv + PWConv	$[B, 48, N]$
	Feature reduction	$[B, 24, N]$
	Distance attention extractor	$[B, 1, N]$
Motion branch	GhostModule + DWConv + PWConv	$[B, 48, N]$
	ECA attention enhancement	$[B, 48, N]$
	Concat (Dist+Motion) $\rightarrow$ FusionBlock	$[B, 48, N]$
Aggregation	Attention-weighted sum	$[B, 48]$
Decoder	2-layer MLP	$[B, 2]$
Reshape + MedianPool	Grid displacement field	$[H/P, W/P, 2]$

Table 4. Estimated MACs per frame of EfficientMotionPro under different keypoint counts  $N$ .

Keypoints $N$	Estimated MACs / frame
128	$\approx 2.14\text{M}$
256	$\approx 4.28\text{M}$
512	$\approx 8.55\text{M}$

a homography-based projection supervision. Specifically, local homography transformations are constructed from the smoothed grid motion field  $S_t$ . The original keypoint positions are then projected using these homographies, and a consistency error is computed against their actual warped positions:

$$\mathcal{L}_{\text{proj}} = \frac{1}{|\Omega_{kp}|} \sum_{p \in \Omega_{kp}} \omega_{t,p} \rho(\mathcal{W}(p; O_t), H_t^{\text{local}}(p; S_t) \cdot p), \quad (23)$$

where  $\rho(\cdot, \cdot)$  denotes the Charbonnier penalty  $\rho(a, b) = \sqrt{\|a - b\|_2^2 + \epsilon^2}$ , and  $H_t^{\text{local}}(p; S_t)$  represents the local homography estimated from the smoothed grid  $S_t$  at point  $p$ . This term effectively enhances the accuracy and geometric plausibility of the smoothed trajectory field at the locations of real keypoints.

**(3) Total Loss** The final optimization objective for the trajectory smoothing module is defined as the weighted combination of all **three** losses:

$$\mathcal{L}_{\text{total}} = \mathcal{L}_{\text{temp}} + \lambda_{\text{spatial}} \mathcal{L}_{\text{spatial}} + \lambda_{\text{proj}} \mathcal{L}_{\text{proj}}, \quad (24)$$

where  $\lambda_{\text{time}} = 20$ ,  $\lambda_{\text{freq}} = 1$ ,  $\lambda_{\text{spatial}} = 10$ , and  $\lambda_{\text{proj}} = 5$  are the default hyperparameters inside/alongside  $\mathcal{L}_{\text{temp}}$  (time/freq) and the two auxiliary terms.

## 9.2. Network Architecture

Fig. 8 illustrates the architecture of our OnlineSmoother network. Given frame-wise displacements, we form a

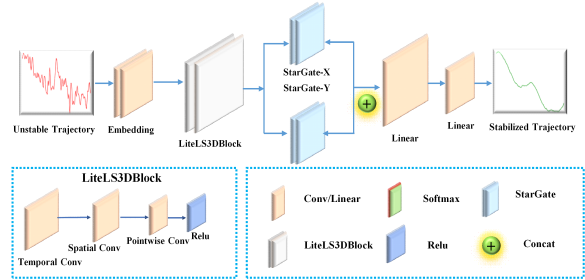


Figure 8. The architecture of our OnlineSmoother network.

causal trajectory tensor  $[B, 2, T, H, W]$  (two channels for  $x/y$ ). **OnlineSmoother** consists of: trajectory encoder (Linear ( $2 \rightarrow 64$ ) + ReLU), spatiotemporal modeling (Lite LS-3D [46]: temporal large-kernel DW-Conv3d + spatial  $1 \times 3 \times 3$  DW-Conv3d, optional  $1 \times 1 \times 1$  PW-Conv3d for mixing), Star-gated [32] dynamic-kernel decoder (two linear heads for gating/amplitude and one scale head), and kernel-guided iterative smoothing. Table 5 summarizes the design.

**(1) Implementation Details** We train and evaluate **OnlineSmoother** on the same self-collected unstable video dataset (with sequence-level train/val splits) that is also used for **EfficientMotionPro**.

Batch size is 1 to preserve causality. Optimizer: Adam ( $\beta_1 = 0.9, \beta_2 = 0.99$ ), weight decay  $1 \times 10^{-5}$ . Learning rate: OneCycleLR with maximum  $2 \times 10^{-4}$ , warm-up for the first 30% steps, then cosine annealing. The smoothing loss combines  $\mathcal{L}_{\text{time}}$ ,  $\mathcal{L}_{\text{spatial}}$ , and  $\mathcal{L}_{\text{proj}}$  with default weights  $(\lambda_{\text{time}}, \lambda_{\text{spatial}}, \lambda_{\text{proj}}) = (20, 10, 5)$  and internal  $\lambda_{\text{freq}} = 1$ . Training runs for 100 epochs; gradient clipping (threshold 5.0) ensures numerical stability.

Validation is performed every 3 epochs; the best model based on the validation loss (Fig. 9) is saved. Training is conducted on a single NVIDIA RTX 4090 GPU (about 2.5 hours).

Table 5. Architecture of the **OnlineSmoother** module. Per-vertex processing; outputs are per-vertex kernels and smoothed trajectories.

Submodule	Tensor Shape (Input $\rightarrow$ Output)	Structural Components
Trajectory Encoder	$[B, 2, T, H, W] \rightarrow [B, 64, T, H, W]$	Linear ( $2 \rightarrow 64$ ) + ReLU
Lite LS-3D (Temporal)	$[B, 64, T, H, W] \rightarrow [B, 64, T, H, W]$	DW-Conv3d ( $k_t \times 1 \times 1$ , dilation $d_t$ ) + ReLU
Lite LS-3D (Spatial)	$[B, 64, T, H, W] \rightarrow [B, 64, T, H, W]$	DW-Conv3d ( $1 \times 3 \times 3$ ) + ReLU
(Optional) Channel Mixing	$[B, 64, T, H, W] \rightarrow [B, 64, T, H, W]$	PW-Conv3d ( $1 \times 1 \times 1$ , groups=4) + ReLU
Kernel Decoder (x)	$[64] \rightarrow [6]$ (per vertex)	Linear (gate), Sigmoid; Linear (amplitude)
Kernel Decoder (y)	$[64] \rightarrow [6]$ (per vertex)	Same as $x$
Scale Decoder (shared)	$[64] \rightarrow [1]$ (per vertex)	Linear (scale)
Kernel Map	$[B, 12, T, H, W]$	Element-wise mult., Star-gated fusion
Kernel-guided Smoothing	$[B, 2, T, H, W] \rightarrow [B, 2, T, H, W]$	Iterative consistency refinement (6-step kernel)

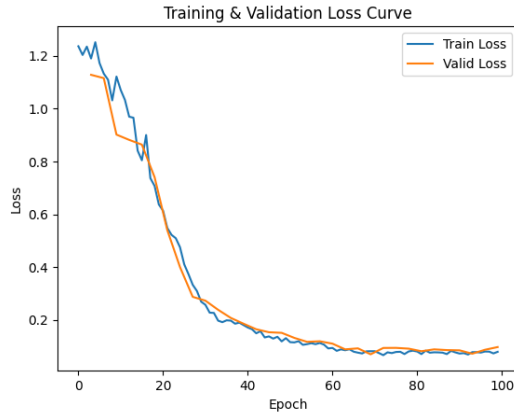


Figure 9. Training curves of **OnlineSmoother**: blue for training loss, orange for validation loss.

## (2) Complexity Analysis

**Parameter Count.** Let  $C = 64$  (embedding dim), temporal kernel  $k_t = 5$ , and optional PW mixing controlled by `use_pointwise`. Counts (approx.): Encoder Linear ( $2 \rightarrow C$ ):  $2C$ ; DW-temporal:  $\mathcal{O}(Ck_t)$ ; DW-spatial:  $\mathcal{O}(9C)$ ; (Opt.) PW-Conv3d (groups=4):  $\approx C^2/4$ ; Star-gated decoder: two Linear ( $C \rightarrow 6$ ) per direction ( $2 \cdot 6C$  each) + one Linear ( $C \rightarrow 1$ ) scale. Total (no PW): for  $C = 64, k_t = 5$  is  $\sim 2.6K$ ; with PW (groups=4) adds  $\sim 1.0K$ , totaling  $\sim 3.6K$ .

**Time Complexity.** Let batch  $B$ , temporal window  $T$ , grid size  $H \times W$ . Dominant MACs (ignoring BN/activations/Sigmoid) come from per-vertex Linear and depthwise 3D convolutions:

$$\mathcal{O}(BTHW \cdot (2C + Ck_t + 9C)) \quad (25)$$

plus decoder heads  $\approx \mathcal{O}(BTHW \cdot 25C)$  and (opt.) PW mixing  $\mathcal{O}(BTHW \cdot C^2/\text{groups})$ . Overall (no PW):

$$\mathcal{O}(BTHW \cdot (2C + Ck_t + 9C + 25C)). \quad (26)$$

Table 6. Estimated MACs of the OnlineSmoother backbone at different grid sizes ( $C = 64, k_t = 5, T = 7, B = 1$ ).

Window $T$	Grid $H \times W$	MACs / frame
7	$16 \times 16$	$\approx 4.6M$
7	$32 \times 32$	$\approx 18.4M$
7	$48 \times 48$	$\approx 41.5M$

Kernel-guided updates with  $R$  rounds and six history steps are scalar-weighted and negligible relative to the forward pass (even with  $R = 20$ ).

**Memory Complexity.** Feature maps are  $[B, C, T, H, W]$ ; kernel heads  $[B, 6, T, H, W]$  and  $[B, 1, T, H, W]$ . Thus memory is  $\mathcal{O}(BCTHW)$ , independent of input image resolution.

**Numerical Estimation (Default  $C = 64, k_t = 5, T = 7$ ).** Ignoring BN/activations/Sigmoid and with  $B = 1$ :

$$\text{MACs} \approx T \cdot H \cdot W \cdot C \cdot (k_t + 35) \quad (27)$$

For  $H = W = 32$ :

$$7 \cdot 32 \cdot 32 \cdot 64 \cdot 40 \approx 18.4M \quad (28)$$

We summarize per-grid costs in Table 6.

## 10. Multi-Threaded Asynchronous Buffering Pipeline: Additional Details

**(1) Motivation and Formulation** Although each individual module is computationally lightweight, executing them in sequence leads to the accumulation of stage latencies:

$$T_{\text{serial}} = t_{\text{est}} + t_{\text{prop}} + t_{\text{smooth}}, \quad (29)$$

where  $t_{\text{est}}$ ,  $t_{\text{prop}}$ , and  $t_{\text{smooth}}$  denote the average per-frame runtimes of the **Motion Estimation**, **Motion Propagation**, and **Motion Compensation** stages, respectively. This serial bottleneck prevents strict real-time performance.

**(2) Pipeline Architecture** To mitigate this, we decompose the stabilization pipeline into three concurrent daemon threads, decoupled by bounded FIFO (First-In-First-Out) shared queues with back-pressure (threads block on empty/full states). This design ensures safe resource handling even under exceptional conditions:

- **T<sub>ME</sub> (Motion Estimation):** Acquires input frames  $I_t$ , performs keypoint collaboration detection  $\mathcal{D}$ , homogenization via SSC, and sparse keypoint-guided causal flow fusion to produce  $\mathbf{m}_t = [x_{kp}; y_{kp}; u; v]$  and the reweighted flow field  $\hat{\mathbf{f}}_{t \leftarrow t-1}$ .
- **T<sub>MP</sub> (Motion Propagation):** Consumes outputs from T<sub>ME</sub>. Executes the EfficientMotionPro network, which computes the multi-homography prior, predicts per-vertex residuals  $\Delta g_{res,t}$  via the lightweight backbone, and outputs the full-frame grid motion field  $\Delta g_t$ .
- **T<sub>MC</sub> (Motion Compensation):** Consumes grid motions  $\Delta g_t$  (or integrated trajectories  $O_t$ ) from T<sub>MP</sub>. Applies the **OnlineSmoother** network for online causal smoothing, yielding the stabilized trajectory  $S_t$ . Finally, it computes the compensation field  $M_t = S_t - O_t$ , performs frame warping via  $\mathcal{W}(x; M_t)$ , and outputs the stabilized frame  $\tilde{I}_t$ .

Threads communicate exclusively through the following shared queues:

$$\begin{aligned}
 Q_{ME \rightarrow MP} : \\
 & \text{Transmits } \mathbf{m}_t \text{ (keypoint motion features),} \\
 & \text{plus metadata,} \\
 Q_{MP \rightarrow MC} : \\
 & \text{Transmits } \Delta g_t \text{ (grid motion field),} \\
 & \text{plus metadata.}
 \end{aligned} \tag{30}$$

**(3) Theoretical Analysis** Let the steady-state per-frame service times be  $\mathbf{t} = (t_{est}, t_{prop}, t_{smooth})$  and the capacity of each queue be  $C$ :

- **Throughput (Steady-State):** The pipeline’s frame rate is bounded by the slowest stage.

$$\begin{aligned}
 \eta_{pipe} &\approx \frac{1}{\max\{t_{est}, t_{prop}, t_{smooth}\}}, \\
 FPS_{max} &\approx \frac{1}{\max\{t_{est}, t_{prop}, t_{smooth}\}}.
 \end{aligned} \tag{31}$$

- **Theoretical Speedup (vs. Serial Execution):**

$$S = \frac{t_{est} + t_{prop} + t_{smooth}}{\max\{t_{est}, t_{prop}, t_{smooth}\}}. \tag{32}$$

- **End-to-End Latency:** The delay for a frame to traverse the entire pipeline is reduced from the serial sum to the duration of the longest stage plus queuing delays, which are minimal for adequately sized buffers.

- **Memory Overhead:** The memory footprint is dominated by the bounded queues.

$$\mathcal{M} = \mathcal{O}(C_{ME} \cdot |\mathbf{m}_t| + C_{MP} \cdot |\Delta g_t|), \tag{33}$$

where  $|\mathbf{m}_t|$  and  $|\Delta g_t|$  represent the size of the data packets transmitted between threads, and  $C_{ME}, C_{MP}$  are the capacities of the respective queues.

#### (4) Complexity and Real-Time Properties

- **Computational Complexity:** Pipeline parallelism does not change the asymptotic complexity  $\mathcal{O}(\cdot)$  of each individual stage; it primarily reduces the wall-clock time from the sum  $t_{est} + t_{prop} + t_{smooth}$  to the maximum  $\max\{t_{est}, t_{prop}, t_{smooth}\}$ .
- **Memory/Bandwidth:** The memory and inter-thread communication bandwidth scale linearly with the chosen queue capacities. This overhead is typically negligible compared to the memory required for processing batches of frames or implementing global buffering and reordering strategies.
- **Real-Time Performance:** If the service times are balanced ( $t_{est} \approx t_{prop} \approx t_{smooth}$ ), the throughput approaches a  $3\times$  speedup over serial execution. If one stage is the dominant bottleneck, the overall throughput is determined by that stage’s processing rate, while the latency for an individual frame is still reduced to approximately the duration of that longest stage.

## 11. Frame Outpainting Details

When the stabilized video is cropped, we first compute the cropping ratio and then determine the scaling required for outpainting. The scaling factors are derived from the cropped dimensions defined by the frame borders.

**Cropping Ratio and Cropped Size** Let  $W_{orig}, H_{orig}$  be the original width and height. Let  $B_{hor}$  and  $B_{ver}$  denote the per-side horizontal (left/right) and vertical (top/bottom) border thickness (in pixels), respectively. Then

$$\begin{aligned}
 W_{cropped} &= W_{orig} - 2B_{hor}, \\
 H_{cropped} &= H_{orig} - 2B_{ver}.
 \end{aligned} \tag{34}$$

The cropping ratio (content preservation) is

$$C = \frac{W_{cropped} H_{cropped}}{W_{orig} H_{orig}} \in (0, 1]. \tag{35}$$

**Scaling Factors for Outpainting** To compensate for the cropped regions, we define the anisotropic scaling factors

$$scale_w = \frac{W_{orig}}{W_{cropped}} = \frac{W_{orig}}{W_{orig} - 2B_{hor}}, \tag{36}$$

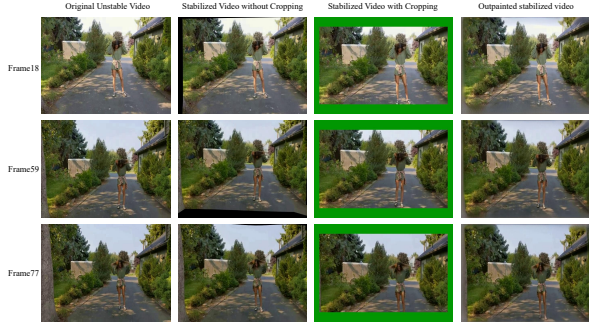


Figure 10. Left to right: Original unstable video; Stabilized (uncropped); Stabilized (cropped); Stabilized (with frame outpainting).

$$\text{scale}_h = \frac{H_{\text{orig}}}{H_{\text{cropped}}} = \frac{H_{\text{orig}}}{H_{\text{orig}} - 2B_{\text{ver}}}. \quad (37)$$

If aspect ratio must be preserved (recommended), use an isotropic factor

$$s = \max(\text{scale}_w, \text{scale}_h) \quad (s \geq 1). \quad (38)$$

**Outpainting with the ProPainter Model** ProPainter [64] is then applied to the missing boundary regions induced by the target scaling. In practice, we first warp each stabilized frame to the outpainted canvas using the chosen factor ( $\text{scale}_w$ ,  $\text{scale}_h$  or  $s$ ), and then invoke ProPainter to fill the uncovered areas near the borders. This preserves the original content while minimizing visible seams at frame boundaries. Figures 10 illustrates the difference between the pre- and post-stabilization video with outpainting.

## 12. Additional Details for UAV-Test Dataset

To comprehensively evaluate robustness and generalization in complex real-world conditions, we construct and release the **UAV-Test** dataset for video stabilization. This dataset captures instability patterns common in aerial operations, such as high-frequency vibrations, aggressive maneuvers, and occlusions. Figures 11 and 12 present sample visible-light and infrared scenes.

**Data Collection Protocol** Data were captured using a DJI Matrice 300 RTK UAV equipped with a DJI Zenmuse H20N gimbal camera, featuring both a wide-angle visible-light sensor and a long-wave infrared sensor. The visible-light lens supports optical zoom from 4.5–360 mm, while the infrared lens (8–14  $\mu\text{m}$ ) has a fixed focal length of 150 mm. The shutter speed was set to automatic, and ISO was set within 100–1600. Videos were recorded at  $1280 \times 720$  and  $1920 \times 1080$  resolutions, with frame rates of 25–30 FPS, simulating varying transmission bandwidths and computational loads.

Table 7. Per-frame runtime comparison on Jetson AGX Orin. We report the average per-frame runtime (ms) and FPS. Our method is significantly faster than MeshFlow, StabNet, and NNDVS, and second only to the highly lightweight Liu et al. [29].

Method	Runtime (ms)	FPS
MeshFlow [28]	168.95	5.92
StabNet [48]	179.88	5.56
NNDVS [58]	340.02	2.94
Liu et al. [29]	36.41	27.47
Ours	78.94	12.67

**Scene Distribution** UAV-Test comprises 92 video sequences totaling  $\sim 26$  minutes, covering five categories:

- **Urban Areas** (19 sequences, 4.5 min): Building circumnavigation and traversal under wind levels 3–4.
- **Highways** (22 sequences, 6.3 min): High-speed parallel tracking under wind levels 2–3.
- **Forested Mountains** (18 sequences, 5.9 min): Canopy penetration and terrain tracking under wind levels 3–5.
- **Waterfronts** (20 sequences, 6.0 min): Disturbance from water-surface reflections under wind levels 3–4.
- **Industrial Sites** (13 sequences, 3.2 min): Occlusions from machinery under wind level 3.

**Annotation and Cleaning** Corrupted frames caused by transmission errors were automatically detected and removed using `ffmpeg`, ensuring clean sequences for evaluation.

**Partitioning and Licensing** UAV-Test is designated as a pure testing set. A stratified sampling strategy based on scene type, weather (sunny/rainy/foggy), and time of day (day/night) ensures diversity. The dataset will be released with source code; access can be requested via email. All flights complied with airspace regulations, and privacy-sensitive information such as human faces and license plates was blurred.

## 13. Runtime Analysis

While many stabilization algorithms achieve real-time performance on high-end GPUs, their efficiency often drops sharply on embedded platforms. To assess practical efficiency, we benchmarked our method on the Jetson AGX Orin and compared it with MeshFlow [28], StabNet [48], NNDVS [58], and Liu et al. [29]. Experimental results show that, thanks to its lightweight architecture and multi-threaded buffering, our method runs at  $\sim 13$  FPS (78.94 ms per frame). This is markedly faster than MeshFlow, StabNet, and NNDVS, and second only to the extremely lightweight approach of Liu et al., demonstrating a

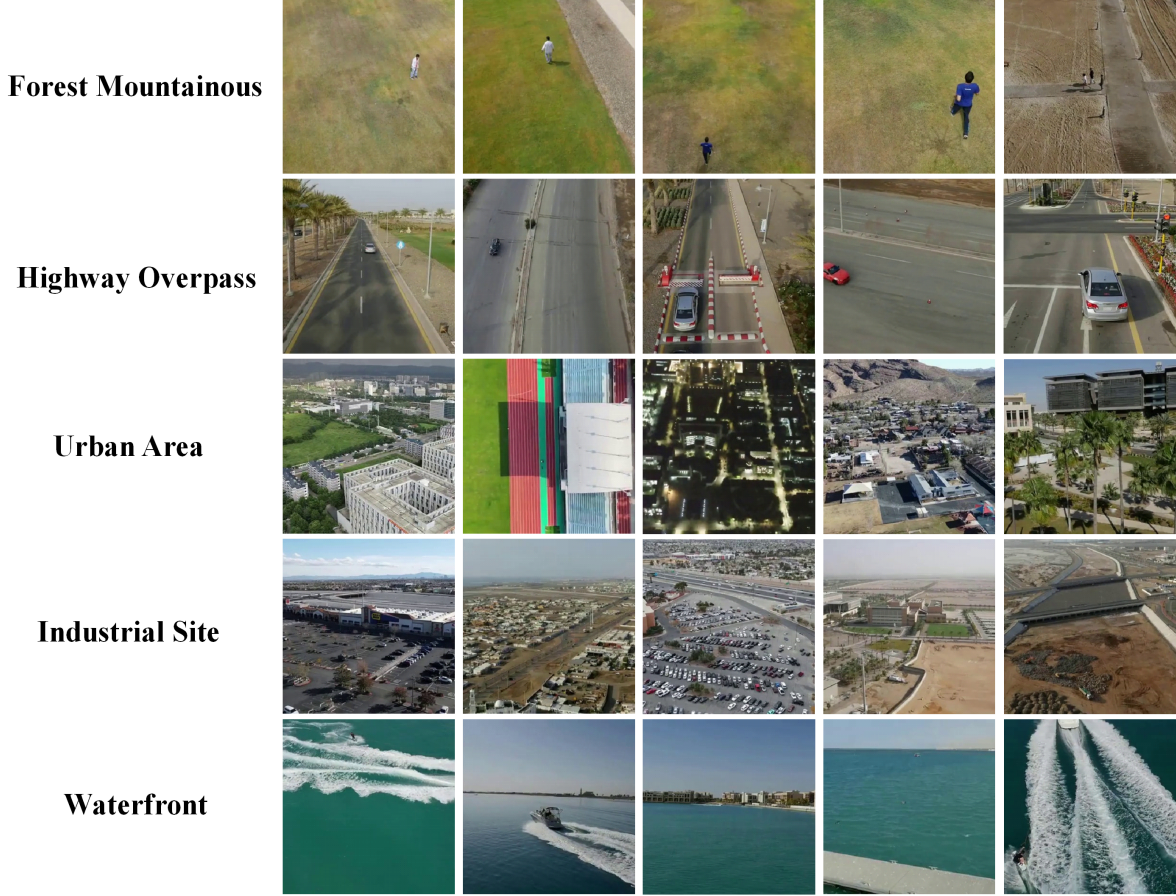


Figure 11. Representative examples of unstable UAV visible-light videos from diverse scenarios, including urban areas, highways, forested mountains, waterfronts, and industrial sites.

favorable trade-off among accuracy, real-time performance, and deployment adaptability. *Note:* all timings exclude the optional frame-outpainting post-processing step; only the time to produce a stabilized frame is measured for every method.

## 14. Evaluation Metrics and Implementation

For reproducibility, we explicitly define the three core metrics used in the main paper, following [27], together with implementation details.

**Cropping Ratio (C)** For each frame, a global homography between the input and the stabilized output is estimated, and the scaling components are used to compute the cropping ratio. The overall cropping ratio  $C$  is defined as the average across all frames. Let the effective field of view after stabilization be  $\Omega_t$  and the original field of view be  $\Omega$ , then:

$$C = \frac{1}{T} \sum_{t=1}^T \frac{|\Omega_t|}{|\Omega|}. \quad (39)$$

**Implementation details.** The cropping ratio is estimated from the scaling factors  $s_x, s_y$  of the frame homography  $H_t$ . To obtain a stricter measure, the four image corners are projected onto the stabilized view, and the preserved ratios along the width and height are computed; the minimum of the two defines the FOV metric, capturing the worst-case preserved region.

**Distortion Value (D)** The distortion value measures anisotropic scaling introduced by the affine part of the homography. Specifically, for each frame  $t$ , let  $\sigma_{\max}(H_t)$  and  $\sigma_{\min}(H_t)$  be the singular values of the estimated homography  $H_t$ . The frame-wise distortion (higher is better) is

$$D_t = \frac{\sigma_{\min}(H_t)}{\sigma_{\max}(H_t)} \in (0, 1]. \quad (40)$$

The global distortion metric  $D$  is defined as the minimum value across all frames, ensuring robustness against outliers:

$$D = \min_t D_t. \quad (41)$$

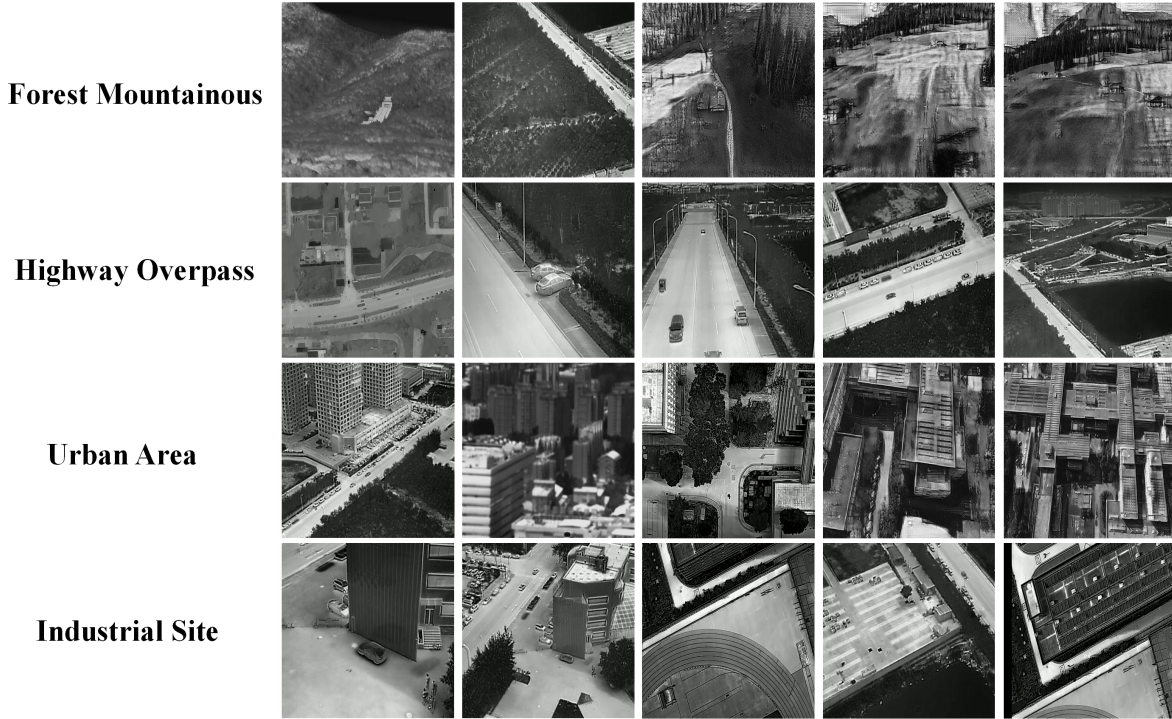


Figure 12. Representative examples of unstable UAV infrared videos from diverse scenarios, including urban areas, highways, forested mountains, and industrial sites.

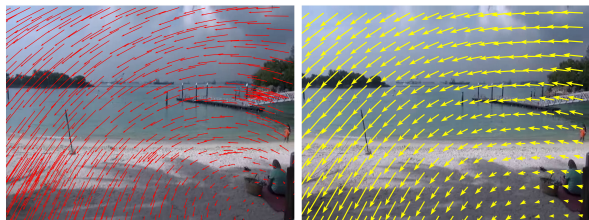


Figure 13. Visualization of motion propagation. The sparse optical flow guided by initial keypoints is contrasted with the grid-wise motion after propagation by our EfficientMotionPro module. The results show that our propagation yields more consistent and structured motion, robust to disturbances caused by dynamic objects and noise.

**Stability Score (S)** The stability score is defined by frequency-domain analysis of the estimated camera trajectory. The translation and rotation components are extracted as 1D temporal signals. The stability score is defined as the proportion of low-frequency energy (2nd–6th order frequencies, excluding the DC component). Formally, let  $X(f)$  denote the Fourier spectrum of the trajectory signal and  $B_{\text{low}}$  the low-frequency band:

$$S = \frac{\sum_{f \in B_{\text{low}}} |X(f)|^2}{\sum_f |X(f)|^2}. \quad (42)$$

**Implementation details.** Trajectories are accumulated frame by frame using relative homographies, from which translation and rotation (approximated by  $\arctan(s_x/s_y)$ ) are extracted. FFT is applied to both translation and rotation sequences. After removing the DC component, the energy ratio of the first five non-zero frequencies (2nd–6th) is computed. The final stability score is the minimum of the translation-based and rotation-based ratios, yielding a strict evaluation.

**PSNR** Peak Signal-to-Noise Ratio (PSNR) is used to measure reconstruction quality in videos and images:

$$\text{PSNR} = 10 \cdot \log_{10} \left( \frac{\text{MAX}_I^2}{\text{MSE}} \right), \quad (43)$$

where  $\text{MAX}_I$  is the maximum possible pixel value (255 for 8-bit images). The mean squared error (MSE) between a reference frame  $I_i$  and a test frame  $K_i$  with  $N$  total pixels is

$$\text{MSE} = \frac{1}{N} \sum_{i=1}^N (I_i - K_i)^2. \quad (44)$$

## 15. Quantitative Evaluation

Fig. 14 presents the per-scene evaluation results for our method and other online approaches on the NUS [26],

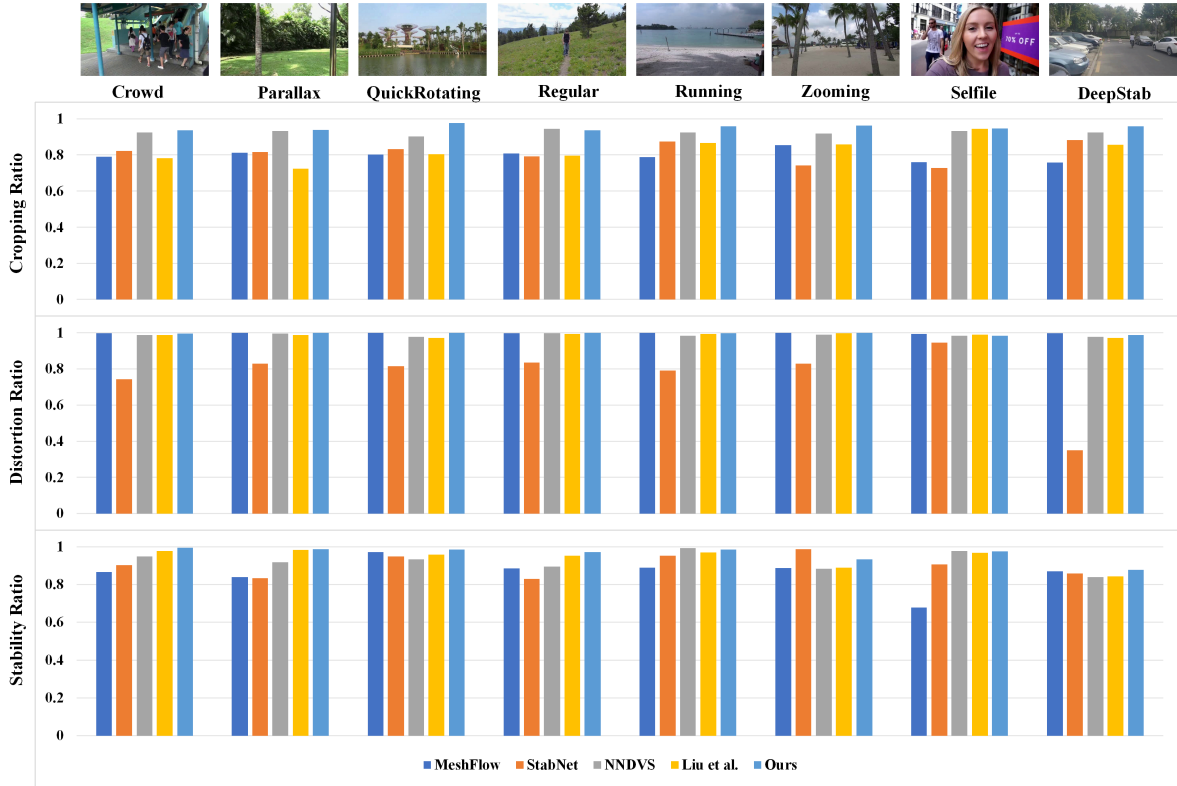


Figure 14. Per-scene quantitative evaluation.

Selfie [57], and DeepStab [48] datasets. Both our method and representative 2D-based full-frame methods [7, 25, 60] achieve the maximum cropping ratio of 1, indicating that the stabilized videos retain the full field of view without cropping. In terms of distortion and stability, our method achieves performance comparable to the state-of-the-art 3D-based method [34], while outperforming 2D-based methods [7, 25, 28, 60]. In summary, the proposed method demonstrates both effectiveness and robustness across diverse scenarios.

## 16. User Study

We conducted a user study via an online SurveyPlus questionnaire. From the five datasets described in the paper, we randomly selected two video sequences from each, resulting in ten short video clips in total. The original unstable videos were synchronized and displayed side-by-side with stabilized outputs generated by four state-of-the-art online methods and our approach. The stabilized videos were arranged in randomized order, with each video potentially appearing in either central or peripheral positions. Participants could replay the videos to ensure a fair comparison. Finally, they were asked to rank the visual quality from best to worst, with the best video assigned 5 points, followed by 4, 3, 2, and 1 point for the worst. Figure 15 illustrates an

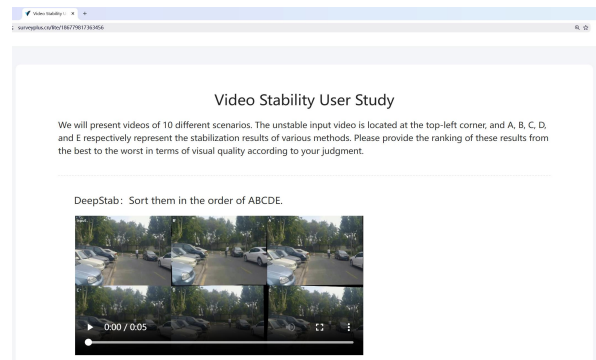


Figure 15. Example question from the user study survey.

example of our questionnaire design.

## 17. Additional Visualization Results

**Motion Visualization** Fig. 13 illustrates the sparse optical-flow motion guided by the initial keypoints and the grid-wise motion obtained after propagation with our **EfficientMotionPro** module. After propagation, the estimated motion remains consistently structured and is less affected by dynamic objects and noise.

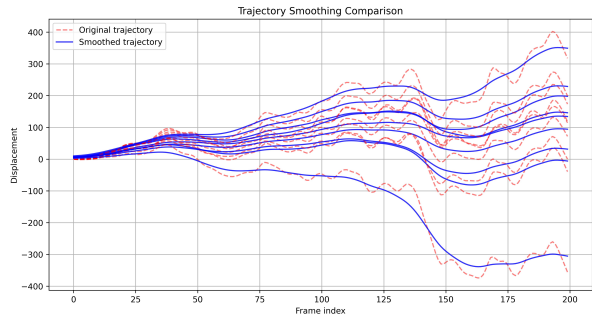


Figure 16. Visualization of mesh vertex trajectories during online smoothing. Six vertices are randomly selected, showing comparisons between unsmoothed trajectories after motion propagation and those refined by our **OnlineSmother**.

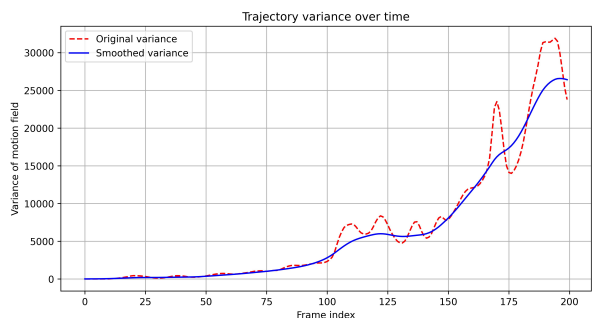


Figure 17. Comparison of trajectory variance before and after applying **OnlineSmother**, demonstrating its effectiveness in suppressing fluctuations.

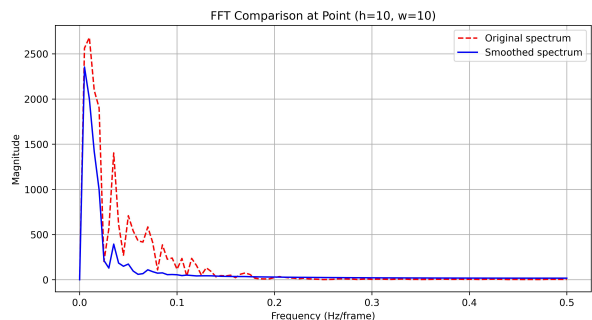


Figure 18. Frequency-domain analysis of trajectories via FFT, highlighting that **OnlineSmother** effectively attenuates high-frequency noise.

**Trajectory Visualization** As illustrated in Figs. 16, 17, and 18, we visualize mesh-vertex trajectories during online smoothing, comparing trajectories obtained after motion propagation without **OnlineSmother** to those refined by **OnlineSmother**. For clarity, we randomly select six mesh vertices to display their smoothed trajectories. We also plot trajectory variance and FFT spectra to further highlight the effectiveness of our **OnlineSmother** module.

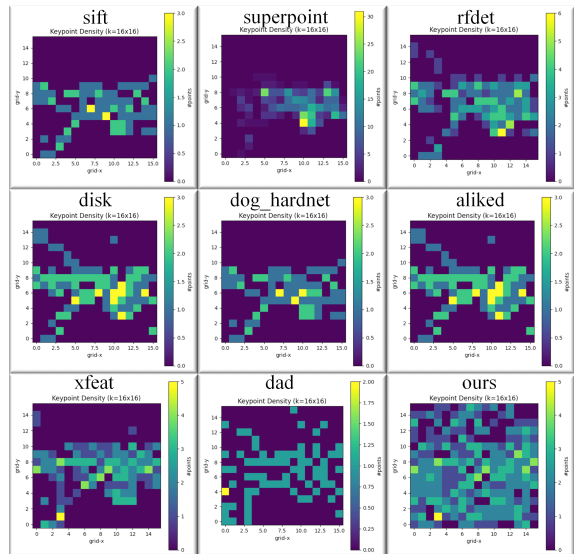


Figure 19. Keypoint density heatmaps of representative detectors (SIFT [31], SuperPoint [8], RFdet [38], DISK [45], DoG-HardNet [6], ALIKED [63], XFeat [35], DAD [11], and Ours) on a sample scene. Our collaborative detector achieves more uniform coverage across the image grid.

**Keypoint Density Visualization** To further illustrate the advantage of our collaborative detector, we visualize keypoint density maps of different detectors in Fig. 19. The heatmaps are computed over a  $16 \times 16$  grid. As shown, traditional and learning-based detectors often produce highly clustered distributions (e.g., SIFT [31] and SuperPoint [8]), whereas our collaborative method yields more uniform spatial coverage, providing a stronger foundation for downstream geometric estimation.

**Optical Flow Visualization** Fig. 20 presents the results of several representative and state-of-the-art optical-flow algorithms, including [4, 9, 17, 39, 41, 43, 59]. In our experiments, we adopt MemFlow [9], which achieves high accuracy while being memory-efficient.

## 18. Video Results

In the supplementary material, we provide a 3-minute comparison video of our online stabilization method against other online methods. This video offers an intuitive view of our method’s behavior across diverse scenarios.

## 19. Limitations

Our method achieves unsupervised online video stabilization through explicit motion estimation and trajectory smoothing. However, there are two main limitations. First, it relies on existing optical-flow estimators, which may be

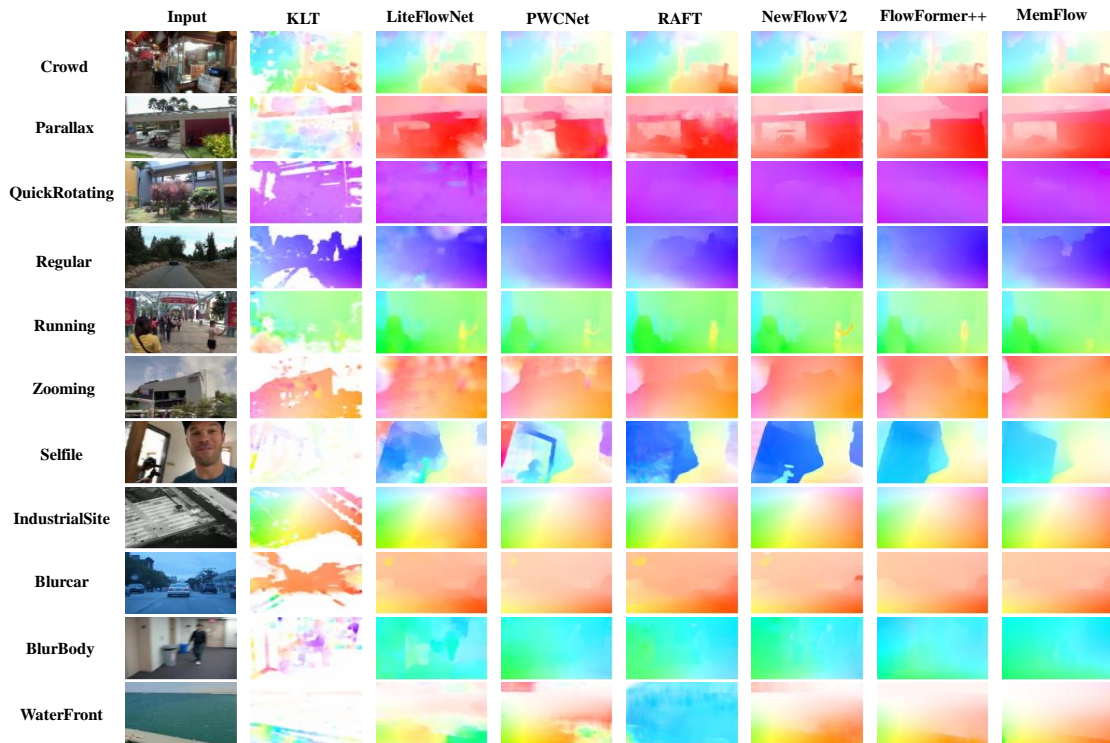


Figure 20. Comparison of representative optical-flow algorithms on diverse examples. We report results from several state-of-the-art methods [4, 9, 17, 39, 41, 43, 59], among which MemFlow [9] is adopted in our experiments for its balance of accuracy and memory efficiency.

less accurate in complex scenes. Second, to improve visual quality, we currently rely on a post-processing frame outpainting step to handle black borders; due to its computational cost, it is not integrated into the online pipeline. To address these issues, we plan to (i) explore more accurate yet efficient optical-flow models, and (ii) develop lighter, online-friendly outpainting techniques that improve edge quality without sacrificing real-time performance.

## References

- [1] Muhammad Kashif Ali, Eun Woo Im, Dongjin Kim, and Tae Hyun Kim. Harnessing meta-learning for improving full-frame video stabilization. In *CVPR*, pages 12605–12614, 2024. 3, 6, 7
- [2] Rana Ashar, Burhan Sadiq, Hira Mohiuddin, Saniya Ashraf, Muhammad Imran, and Anayat Ullah. Video stabilization using raft-based optical flow. In *ICRAI*, pages 1–5, 2023. 3
- [3] Oleksandr Bailo, Francois Rameau, Kyungdon Joo, Jinsun Park, Oleksandr Bogdan, and In So Kweon. Efficient adaptive non-maximal suppression algorithms for homogeneous spatial keypoint distribution. *PRL*, 106:53–60, 2018. 4
- [4] Simon Baker and Iain Matthews. Lucas-kanade 20 years on: A unifying framework. *IJCV*, 56(3):221–255, 2004. 18, 19
- [5] Jonathan T Barron. A general and adaptive robust loss function. In *CVPR*, pages 4331–4339, 2019. 5
- [6] Ping Chao, Chao-Yang Kao, Yu-Shan Ruan, Chien-Hsiang Huang, and Youn-Long Lin. Hardnet: A low memory traffic network. In *ICCV*, pages 3552–3561, 2019. 18
- [7] Jinsoo Choi and In So Kweon. Deep iterative frame interpolation for full-frame video stabilization. *ACM TOG*, 39(1): 1–9, 2020. 1, 3, 6, 7, 17
- [8] Daniel DeTone, Tomasz Malisiewicz, and Andrew Rabinovich. Superpoint: Self-supervised interest point detection and description. In *CVPRW*, pages 224–236, 2018. 3, 18
- [9] Qiaole Dong and Yanwei Fu. Memflow: Optical flow estimation and prediction with memory. In *CVPR*, pages 19068–19078, 2024. 3, 4, 18, 19
- [10] Alexey Dosovitskiy, Philipp Fischer, Eddy Ilg, Philip Hausser, Caner Hazirbas, Vladimir Golkov, Patrick Van Der Smagt, Daniel Cremers, and Thomas Brox. FlowNet: Learning optical flow with convolutional networks. In *ICCV*, pages 2758–2766, 2015. 3
- [11] Johan Edstedt, Georg Bökman, Mårten Wadenbäck, and Michael Felsberg. DaD: Distilled reinforcement learning for diverse keypoint detection. *arXiv preprint arXiv:2503.07347*, 2025. 3, 18
- [12] Amit Goldstein and Raanan Fattal. Video stabilization using epipolar geometry. *ACM TOG*, 31(5):1–10, 2012. 1
- [13] Matthias Grundmann, Vivek Kwatra, and Irfan Essa. Auto-directed video stabilization with robust l1 optimal camera paths. In *CVPR*, pages 225–232, 2011. 1, 3, 6, 7

- [14] Kai Han, Yunhe Wang, Qi Tian, Jianyuan Guo, Chunjing Xu, and Chang Xu. Ghostnet: More features from cheap operations. In *CVPR*, pages 1580–1589, 2020. 5, 9
- [15] Berthold K. P. Horn and Brian G. Schunck. Determining optical flow. *AI*, 17(1-3):185–203, 1981. 3
- [16] Zhaoyang Huang, Xiaoyu Shi, Chao Zhang, Qiang Wang, Ka Chun Cheung, Hongwei Qin, Jifeng Dai, and Hongsheng Li. Flowformer: A transformer architecture for optical flow. In *ECCV*, 2022. 3
- [17] Tak-Wai Hui, Xiaoou Tang, and Chen Change Loy. Lite-flownet: A lightweight convolutional neural network for optical flow estimation. In *CVPR*, pages 8981–8989, 2018. 18, 19
- [18] Eddy Ilg, Nikolaus Mayer, Tonmoy Saikia, Margret Keuper, Alexey Dosovitskiy, and Thomas Brox. Flownet 2.0: Evolution of optical flow estimation with deep networks. In *CVPR*, pages 2462–2470, 2017.
- [19] Shihao Jiang, Dylan Campbell, Yao Lu, Hongdong Li, and Richard Hartley. Learning to estimate hidden motions with global motion aggregation. In *ICCV*, pages 9772–9781, 2021. 3
- [20] Pierre-Marc Jodoin, Lucia Maddalena, Alfredo Petrosino, and Yi Wang. Extensive benchmark and survey of modeling methods for scene background initialization. *IEEE TIP*, 26(11):5244–5256, 2017. 10
- [21] Levent Karacan and Mehmet Sarigül. Full-frame video stabilization via spatiotemporal transformers. *Computational Visual Media*, 11(3):655–667, 2025. 3, 6, 7
- [22] Abdulrahman Kerim, Washington L. S. Ramos, Leandro Soriano Marcolino, Erickson R. Nascimento, and Richard Jiang. Leveraging synthetic data to learn video stabilization under adverse conditions. In *IEEE WACV*, pages 6931–6940, 2024. 1
- [23] Yao-Chih Lee, Kuan-Wei Tseng, Yu-Ta Chen, Chien-Cheng Chen, Chu-Song Chen, and Yi-Ping Hung. 3d video stabilization with depth estimation by cnn-based optimization. In *CVPR*, pages 10621–10630, 2021. 1, 3, 6, 7
- [24] Feng Liu, Michael Gleicher, Hailin Jin, and Aseem Agarwala. Content-preserving warps for 3d video stabilization. *ACM TOG*, 28(3):223–231, 2009. 1
- [25] Feng Liu, Michael Gleicher, Jue Wang, Hailin Jin, and Aseem Agarwala. Subspace video stabilization. *ACM TOG*, 30(1):1–10, 2011. 1, 17
- [26] Shuaicheng Liu, Lu Yuan, Ping Tan, and Jian Sun. Bundled camera paths for video stabilization. *ACM TOG*, 32(4):1–10, 2013. 1, 3, 6, 7, 16
- [27] Shuaicheng Liu, Lu Yuan, Ping Tan, and Jian Sun. Steadyflow: Spatially smooth optical flow for video stabilization. In *CVPR*, pages 4209–4216, 2014. 1, 15
- [28] Shuaicheng Liu, Ping Tan, Lu Yuan, Jian Sun, and Bing Zeng. Meshflow: Minimum latency online video stabilization. In *ECCV*, pages 800–815, 2016. 1, 3, 6, 7, 14, 17
- [29] Tao Liu, Gang Wan, Hongyang Bai, Xiaofang Kong, Bo Tang, and Fangyi Wang. Real-time video stabilization algorithm based on superpoint. *IEEE TIM*, 73:1–13, 2024. 1, 6, 7, 14
- [30] Yu-Lun Liu, Wei-Sheng Lai, Ming-Hsuan Yang, Yung-Yu Chuang, and Jia-Bin Huang. Hybrid neural fusion for full-frame video stabilization. In *ICCV*, pages 2299–2308, 2021. 3, 6, 7
- [31] David G Lowe. Distinctive image features from scale-invariant keypoints. *IJCV*, 60(2):91–110, 2004. 1, 3, 18
- [32] Xu Ma, Xiyang Dai, Yue Bai, Yizhou Wang, and Yun Fu. Rewrite the stars. In *CVPR*, pages 5694–5703, 2024. 10, 11
- [33] Y. Matsushita, E. Ofek, Weina Ge, Xiaoou Tang, and Heung-Yeung Shum. Full-frame video stabilization with motion inpainting. *IEEE TPAMI*, 28(7):1150–1163, 2006. 1
- [34] Zhan Peng, Xinyi Ye, Weiye Zhao, Tianqi Liu, Huiqiang Sun, Baopu Li, and Zhiguo Cao. 3d multi-frame fusion for video stabilization. In *CVPR*, pages 7507–7516, 2024. 3, 6, 7, 17
- [35] Guilherme Potje, Felipe Cadar, André Araujo, Renato Martins, and Erickson R Nascimento. Xfeat: Accelerated features for lightweight image matching. In *CVPR*, pages 2682–2691, 2024. 3, 18
- [36] Edward Rosten and Tom Drummond. Machine learning for high-speed corner detection. In *ECCV*, pages 430–443, 2006. 1, 3
- [37] Ethan Rublee, Vincent Rabaud, Kurt Konolige, and Gary Bradski. Orb: An efficient alternative to sift or surf. In *ICCV*, pages 2564–2571, 2011. 1, 3
- [38] Xuelun Shen, Cheng Wang, Xin Li, Zenglei Yu, Jonathan Li, Chenglu Wen, Ming Cheng, and Zijian He. RF-net: An end-to-end image matching network based on receptive field. In *CVPR*, pages 8132–8140, 2019. 3, 18
- [39] Xiaoyu Shi, Zhaoyang Huang, Dasong Li, Manyuan Zhang, Ka Chun Cheung, Simon See, Hongwei Qin, Jifeng Dai, and Hongsheng Li. Flowformer++: Masked cost volume autoencoding for pretraining optical flow estimation. In *CVPR*, pages 1599–1610, 2023. 3, 18, 19
- [40] Zhenmei Shi, Fuhao Shi, Wei-Sheng Lai, Chia-Kai Liang, and Yingyu Liang. Deep online fused video stabilization. In *CVPR*, pages 1250–1258, 2022. 3, 6, 7
- [41] Deqing Sun, Xiaodong Yang, Ming-Yu Liu, and Jan Kautz. Pwc-net: Cnns for optical flow using pyramid, warping, and cost volume. In *CVPR*, pages 8934–8943, 2018. 3, 18, 19
- [42] Jiaming Sun, Zehong Shen, Yuang Wang, Hujun Bao, and Xiaowei Zhou. Loftr: Detector-free local feature matching with transformers. In *CVPR*, pages 8922–8931, 2021. 3
- [43] Zachary Teed and Jia Deng. Raft: Recurrent all-pairs field transforms for optical flow. In *ECCV*, pages 402–419, 2020. 3, 18, 19
- [44] Du Tran, Lubomir Bourdev, Rob Fergus, Lorenzo Torresani, and Manohar Paluri. Learning spatiotemporal features with 3d convolutional networks. In *ICCV*, pages 4489–4497, 2015. 1
- [45] Michał Tyszkiewicz, Pascal Fua, and Eduard Trulls. Disk: Learning local features with policy gradient. *NeurIPS*, 33: 14254–14265, 2020. 3, 18
- [46] Ao Wang, Hui Chen, Zijia Lin, Jungong Han, and Guiguang Ding. Lsnet: See large, focus small. In *CVPR*, pages 9718–9729, 2025. 10, 11

- [47] Fangyi Wang, Bihua Zhong, Tao Liu, Xiaofang Kong, Hongyang Bai, and Gang Wan. Deep matching online video stabilization using tsnet. *IEEE TIM*, 73(1):1–13, 2024. [5](#)
- [48] Miao Wang, Guo-Ye Yang, Jin-Kun Lin, Song-Hai Zhang, Ariel Shamir, Shao-Ping Lu, and Shi-Min Hu. Deep online video stabilization with multi-grid warping transformation learning. *IEEE TIP*, 28(5):2283–2292, 2019. [1](#), [2](#), [3](#), [6](#), [7](#), [14](#), [17](#)
- [49] Qilong Wang, Banggu Wu, Pengfei Zhu, Peihua Li, Wang-meng Zuo, and Qinghua Hu. Eca-net: Efficient channel attention for deep convolutional neural networks. In *CVPR*, pages 11534–11542, 2020. [5](#), [9](#)
- [50] Yifan Wang, Xingyi He, Sida Peng, Dongli Tan, and Xiaowei Zhou. Efficient lofr: Semi-dense local feature matching with sparse-like speed. In *CVPR*, pages 21666–21675, 2024. [3](#)
- [51] Yu Shuen Wang, Feng Liu, Pu Sheng Hsu, and Tong Yee Lee. Spatially and temporally optimized video stabilization. *IEEE TVCG*, 19(8):1354–1361, 2013. [1](#)
- [52] Yufei Xu, Jing Zhang, Stephen J. Maybank, and Dacheng Tao. Dut: Learning video stabilization by simply watching unstable videos. *IEEE TIP*, 31:4306–4320, 2022. [1](#), [3](#), [6](#), [7](#)
- [53] Nianjin Ye, Chuan Wang, Shuaicheng Liu, Lanpeng Jia, Jue Wang, and Yongqing Cui. DeepMeshFlow: Content adaptive mesh deformation for robust image registration. *arXiv preprint arXiv:1912.05131*, 2019. [1](#)
- [54] Zinuo You, Stamatios Georgoulis, Anpei Chen, Siyu Tang, and Dengxin Dai. Gavs: 3d-grounded video stabilization via temporally-consistent local reconstruction and rendering. In *Proceedings of the ACM SIGGRAPH 2025 Conference*, 2025. [3](#), [6](#), [7](#)
- [55] Jiyang Yu and Ravi Ramamoorthi. Robust video stabilization by optimization in cnn weight space. In *CVPR*, pages 3800–3808, 2019. [3](#)
- [56] Jiyang Yu and Ravi Ramamoorthi. Learning video stabilization using optical flow. In *CVPR*, pages 8159–8167, 2020. [1](#), [3](#), [6](#), [7](#)
- [57] Jiyang Yu, Ravi Ramamoorthi, Keli Cheng, Michel Sarkis, and Ning Bi. Real-time selfie video stabilization. In *CVPR*, pages 12036–12044, 2021. [1](#), [6](#), [7](#), [17](#)
- [58] Zhuofan Zhang, Zhen Liu, Ping Tan, Bing Zeng, and Shuaicheng Liu. Minimum latency deep online video stabilization. In *ICCV*, pages 23030–23039, 2023. [1](#), [3](#), [5](#), [6](#), [7](#), [14](#)
- [59] Zhiyong Zhang, Huaizu Jiang, and Hanumant Singh. Neuflow: Real-time, high-accuracy optical flow estimation on robots using edge devices. In *IEEE IROS*, pages 5048–5055, 2024. [3](#), [18](#), [19](#)
- [60] Minda Zhao and Qiang Ling. Pwstabenet: Learning pixel-wise warping maps for video stabilization. *IEEE TIP*, 29: 3582–3595, 2020. [1](#), [3](#), [6](#), [7](#), [17](#)
- [61] Weiyue Zhao, Xin Li, Zhan Peng, Xianrui Luo, Xinyi Ye, Hao Lu, and Zhiguo Cao. Fast full-frame video stabilization with iterative optimization. In *CVPR*, pages 23534–23544, 2023. [3](#)
- [62] Xiaoming Zhao, Xingming Wu, Jinyu Miao, Weihai Chen, Peter C. Y. Chen, and Zhengguo Li. Alike: Accurate and lightweight keypoint detection and descriptor extraction. *IEEE TMM*, 25:3101–3112, 2022. [3](#)
- [63] Xiaoming Zhao, Xingming Wu, Weihai Chen, Peter C. Y. Chen, Qingsong Xu, and Zhengguo Li. Aliked: A lighter keypoint and descriptor extraction network via deformable transformation. *IEEE TIM*, 72:1–16, 2023. [3](#), [18](#)
- [64] Shangchen Zhou, Chongyi Li, Kelvin C.K Chan, and Chen Change Loy. Propainter: Improving propagation and transformer for video inpainting. In *ICCV*, pages 10477–10486, 2023. [6](#), [14](#)
- [65] Pengfei Zhu, Longyin Wen, Dawei Du, Xiao Bian, Heng Fan, Qinghua Hu, and Haibin Ling. Detection and tracking meet drones challenge. *IEEE TPAMI*, 44(11):7380–7399, 2021. [10](#)
- [66] Yabin Zhu, Qianwu Wang, Chenglong Li, Jin Tang, Chengjie Gu, and Zhixiang Huang. Visible-thermal multiple object tracking: Large-scale video dataset and progressive fusion approach. *PR*, 161:111330, 2025. [10](#)